FourStar: The Near-Infrared Imager for the 6.5-m Baade Telescope at Las Campanas Observatory

S. E. Persson[1], D. C. Murphy[1], S. Smee[2], C. Birk[1], A. J. Monson[1], A. Uomoto[1], E. Koch[3], S. Shectman[1], R. Barkhouser[2], J. Orndorff[2], R. Hammond[2], A. Harding[2], G. Scharfstein[4], D. Kelson[1], J. Marshall[5], & P. J. McCarthy[1]

persson@obs.carnegiescience.edu, david@obs.carnegiescience.edu, smee@pha.jhu.edu, birk@obs.carnegiescience.edu, amonson@obs.carnegiescience.edu, au@obs.carnegiescience.edu, koch1270@yahoo.com, shec@obs.carnegiescience.edu, rhb@pha.jhu.edu, jdo@pha.jhu.edu, rph@pha.jhu.edu, harding@pha.jhu.edu, gregory.scharfstein@flexureengineering.com, kelson@obs.carnegiescience.edu, marshall@physics.tamu.edu, pmc2@gmto.org

Received _____; accepted _____

[1]Carnegie Observatories, 813 Santa Barbara Street, Pasadena, CA 91101

[2]Instrument Development Group, Johns Hopkins University, Baltimore, MD 21218

[3]Dedicated Micro Systems, Inc., 3095 NE Nathan Dr., Bend, OR 97701

[4]Flexure Engineering, 1285 66th Street, Suite 200, Emeryville, CA 94608

[5]Department of Physics and Astronomy, Texas A&M University, College Station, TX 77843

ABSTRACT

The FourStar Infrared Camera is a 4K × 4K near-infrared (1.0 - 2.4 μm) imager built for the Magellan 6.5 m Baade Telescope at Las Campanas Observatory, Chile. FourStar has an all-refractive optical system, four HAWAII-2RG detectors, and Teledyne electronics. The pixel scale of $0\farcs159$ pixel^{-1} produces a $10\farcm8 \times 10\farcm8$ field of view. Ten filters are available across the Y, J, H, and K_s bands. We present the optical, mechanical, thermal, electronic, and software design choices and their associated engineering implementations. The detector readout electronics, control system, and the automatic data acquisition hardware are also described. Laboratory and on-sky performance data are presented. FourStar has excellent image quality, easily meeting the requirement of critically sampling the median seeing disk. The throughput is ≈ 0.5 - 0.6 across its wavelength coverage. Some early science results are presented.

Subject headings: Astronomical Instrumentation

1. Introduction

The advent of 2048 × 2048 near-infrared (NIR) detectors has led to the construction of several cameras and spectrographs at major observatories[1]. This paper describes FourStar, a camera mounted on the East Nasmyth focus of the Baade 6.5-m Telescope at Las Campanas Observatory. It is an all-refractive camera operating between 1 and 2.4 μm. Its plate scale is $0\farcs159$ pixel^{-1}giving it a $10\farcm8 \times 10\farcm8$ field of view (FOV). Table 1 lists the basic detector and camera parameters. This instrument should have wide applicability, but specifically it opens up the possibility of carrying out moderate area, deep surveys. One example of a project we are presently pursuing follows van Dokkum et al. (2009) who have used NEWFIRM (Autry et al. 2003) to carry out a survey designed to measure the detailed properties z < 4 galaxies; they have used a set of medium-band filters to determine photometric redshifts, and have thus been able to measure luminosities, star formation rates, masses and environments of many thousands of galaxies in a single pointing. Such galaxies are far too faint to follow up with current infrared spectrographs as discussed by van Dokkum et al. (2009).

The most important design choices were dictated by four considerations. First, the site plus telescope deliver excellent image quality with a NIR full width at half maximum (FWHM) of $\sim 0\farcs5$. We wanted a pixel scale which would not undersample the median FWHM. The exact choice of pixel scale was bounded by our desire to have as large a field as possible, while approximately Nyquist sampling the best quartile of the seeing profile, which is $\sim 0\farcs35$ FWHM at K_s. This indicates a scale close to $\sim 0\farcs16$ pixel^{-1} for a nominal 18 μm pixel. Thus the camera must reduce the $f/11$ telescope beam at the image plane to $f/3.6$ at the detector.

[1]e.g., VISTA at ESO, HAWK-I at ESO, NEWFIRM at NOAO, MMIRS at LCO, among others.

Second, funding constraints, together with the image and detector f–ratios, led directly to a design based on a detector mosaic of four 2K × 2K detectors arranged in a close format. The beam at the Nasmyth port of Baade has a plate scale of $2\farcs88$ mm^{-1}. This implies $\sim$ 35 cm footprint at the camera entrance window and correspondingly large optics and cryogenic volume. These facts taken together led to the parameters of the adopted optical design, and consequently those of the mechanical and thermal designs.

Third, we decided to operate the camera to $\lambda = 2.4$ μm. This single choice greatly increases an instrument's cost and complexity (over that of a camera operating out only into the H band) due to thermal and optical design constraints. Baffling of thermal radiation from the high-emissivity areas within the telescope is basic to good performance at K_s. An effective internal baffle also automatically ensures a system that is well-baffled against sky radiation (particularly OH emission in the J and H bands), to which the focal plane is directly exposed on unbaffled telescopes. Thus the baffle and optics were to be operated at a temperature sufficiently low that the instrument would be background limited, where the background is from the sky and unavoidable sources from within the telescope, e.g., the mirrors. Corresponding designs are of course far more difficult for instruments whose response extends to 5 μm; we decided early on to forgo the longer wavelengths.

Fourth, we chose to use the HAWAII-2RG[2] (H2RG) HgCdTe detectors that Teledyne Scientific & Imaging[3] were then developing. The Teledyne detectors operate at 77 K, have an 18.0 μm pixel pitch, and cutoff at $\lambda \sim 2.5$ μm. The rationale for this decision is discussed in §3 below.

---

[2]HAWAII-2RG stands for [H]gCdTe [A]stronomy [W]ide [A]rea [I]nfrared [I]mager with [2] × 2K pixels, [R]eference pixels and [G]uide Mode.

[3]Table 2 contains a list of all the manufacturers/suppliers of devices used in the project.

These choices led in turn to many practical considerations. As is usual in the design of large cryogenic instruments, the main optomechanical/thermal tradeoffs are between mounting the optics carefully and stiffly, but without introducing excessive heat loads. There are, however, other factors, the most important of which is the safety and handling of the detectors and associated electronics. The dangers to these devices are electrostatic discharge (ESD), rapid temperature cycling, mechanical stresses, and contamination. Each of these required that we handle the detectors as little as possible, follow strict ESD protection procedures, and develop benign and robust cooling and warming procedures. Early estimates indicated that cooling or warming the dewar would take several days, so a further design constraint was to minimize the number of such cycles, especially at the telescope. Ultimately our goal was to maintain the instrument at cryogenic temperatures and ready for operation for many months at a time.

The instrument hardware, software, and operating methods were designed by Carnegie Observatories' scientists and engineers and Instrument Development Group (IDG) engineers at the Johns Hopkins University. We embarked on the design in 2004 and did the integration and testing at Carnegie. It was shipped to Las Campanas in August 2010 and saw first light in December 2010. After a 6-month commissioning period, astronomers were able to start regular observations. As a facility instrument, it is available to all members of the Magellan scientific community.

This paper fully discusses the FourStar instrument. We describe the optical design, optomechanical and thermal designs, mechanisms, electronics, control and data acquisition systems, detector control system, and software design. The automatic data reduction pipeline is incomplete and will be presented later. Following those sections of the paper we present and discuss our measured laboratory and on-telescope performance parameters.

2. Overview

What follows is a general description of the mechanical aspects of the instrument. Figure 1 shows a cutaway view with the optical path in orange. Starting from the left, the instrument bolts via a conical adapter to the (telescope-provided) instrument rotator and XY offset guider (not shown; henceforth the guider). The vacuum vessel, to the right of the window field lens assembly, is shown in blue. After traversing the entrance window and camera optics (four lenses mounted in a Camera Module, henceforth the CM), the light passes through filters mounted in two wheels and the field-flattener wheel before arriving at the detector. Two LN_2 dewars maintain two thermal regimes, one for the focal plane mechanisms, detectors, and internal electronics, and one for the CM optics and radiation shield. The former surrounds the detector dewar at 77 K, and the latter surrounds the CM at $\sim$ 200 K, and extends up to the entrance window. These two temperature regimes are maintained by adjusting the heat flow across three thermal resistors in the form of copper braids. The radiation shield LN_2 reservoir is a circular tank with its fill tube located on the rotation axis so it can be filled automatically. The smaller detector dewar has an off-axis fill-tube; it is filled manually. FourStar is a heavy (910 kg) and long instrument (3 m). Because of this, suspending it from the Nasmyth guider was rejected in favor of offloading most of the weight onto the Nasmyth platform, using the conical attachment to the instrument mounting ring/guider to precisely locate the instrument in space. The vacuum vessel is thus supported at two places - the instrument guider flange and by the astatic support (via rollers) the load ring lying at the center-of-gravity of the CM. The astatic support mechanism is part of the instrument handling cart.

The mechanisms (e.g., filter wheels) are operated via feedthroughs with motors and encoders located outside the vessel and home switches located inside (one mechanism has an internal encoder). The control electronics (motors, switches, temperature controllers,

detector readout computers, communications) are mounted in two thermally insulated sealed enclosures (Electronic Racks in Figure 1) attached to the front section of the instrument. The heat generated from these enclosures is removed by a chilled water/glycol heat exchanger. All control signals including data transfer are sent via a fiber pair to a control computer located on the ground floor of the telescope building. Also located there is a computer cluster designed to process incoming frames automatically so as to provide the observer with a rapid indication of data quality. The observer interacts with the instrument by taking exposures with given filters, running observing macros, and monitoring reduced data in real time.

The FourStar website (http://instrumentation.obs.carnegiescience.edu/FourStar/) contains extensive details on the instrument and its performance. Figure 2 shows the completed instrument resting on its support cart and attached to the Instrument Rotator. The white boom attached to the back of the cart supports piping for a LN_2 autofill system.

3. The Selection of Teledyne HAWAII-2RG Detectors and SIDECAR ASIC Electronics

The decision to use the H2RG detectors (e.g., Beletic et al. 2008, Loose et al. 2003b, 2007, Blank et al. 2011) was made early in the design of FourStar and was based in part on our familiarity with their earlier, smaller devices. Having had previous success with the Teledyne detectors with respect to read noise, bad pixel count, dark current, and quantum efficiency (QE), this was a straightforward choice. Our science-grade detectors were selected from several available on the basis of read noise, cosmetic quality, and QE. These detectors can be read out in two modes: in four quadrants or in 32 channels, each a column 64 pixels wide. We only use the 32-channel mode.

We also decided to adopt the Teledyne SIDECAR[4] ASIC[5] and its associated Teledyne-supplied support hardware and firmware (e.g., Loose et al. 2003a, 2006). This ASIC, originally developed for the James Webb Space Telescope project, is also offered as a product for ground-based users. It runs micro-code written by Teledyne and this controls clocking signals sent to the detector, 32 channels in parallel at a time. The pixel voltages are biased, amplified, digitized, and read out. A variety of choices for amplification gain and other parameters are available.

Our choice to use the ASIC was made for several reasons: first, they promised high performance from a noise perspective. Second, we judged their adoptiion would be easier, far cheaper, and considerably less cumbersome than developing 128 channels of low-noise amplification, A/D conversion, and associated electronics. The prospect of having virtually all the critical detector electronics provided on four small cards seemed greatly preferable to doing this in-house. Our experience has proven this decision correct.

The H2RG/ASIC system supports (in principle) on-chip guiding. We chose to forgo this capability for the present time and use only the telescope guider system.

4. Optical Design

FourStar is a seven-element refractive reimager. The optical layout and prescription[6] are shown in Figure 3 and Table 3[7]. The first two elements (L1, L2) comprise a fused

[4][S]ystem for [I]mage [D]igitization [E]nhancement [C]ontrol [A]nd [R]etrieval].

[5][A]pplication [S]pecific [I]ntegrated [C]ircuit.

[6]All raytracing optimizations were done with ZEMAX.

[7]All dimensions in Table 3 are for the operating temperatures, not for the warmed-up manufacturing case.

silica doublet field lens which forms a 130 mm diameter pupil image 27 mm in front of the subsequent element L3. L1 also serves as the vacuum window and is located 210 mm behind the telescope focal plane so that any dust contamination on the outside surface is significantly out of focus. Three important factors motivated the doublet field lens design. The principal one was to add degrees of freedom for field correction. Second, improved quality of the pupil image was achieved, and third, condensation on L1 was mitigated (see below). The pupil image still suffers from chromatic aberration across the Y, J, H, and K_s bands; the separation of the J and K_s best pupil foci is 51 mm and the blur circle in the K_s band is $\sim$ 2 mm FWHM at the pupil. This is 1.5% of the pupil image diameter.

Most of the optical power for the reimager is provided by a CaF_2/S-FTM16 doublet (L3, L4) followed by two CaF_2 singlets (L5, L6). The negative power in L4 serves to achromatize positive power in the three CaF_2 elements (L3, L5, L6). The front surface of L3 is a diamond-turned asphere which contributes substantially to the image quality and thus FOV. The final element (L7) is a S-TIH1 field flattener. To achieve the highest possible image quality, three separate field flatteners are mounted in a wheel for use in the (Y and J), H, and K_s bands, with slightly different optical prescriptions, but the same final focal position. Each has a band-specific anti-reflection coating to maximize throughput and minimize multiple reflections (ghosts).

Figures 4 and 5 show spot and encircled energy diagrams for the design. Either representation of the modeled image quality shows that a very large percentage (90%) of the energy should be captured within 1.5 pixels all across the field; the predicted optical quality compares favorably with the diffraction limit.

Distortion is small, but not negligible, in this design. The distortion is defined as 100 $\times$ (y_{chief} - y_{ref}) / y_{ref}, where y_{chief} is the ray height of a real traced chief ray and y_{ref} is the ray height of an ideal paraxial ray. ZEMAX predicts wavelength-dependent distortion

values of 1.018, 1.011, and 0.976% at J, H, and K_s respectively, at the corners of the field. Corrections for distortion in the data reduction process must be done accurately, i.e., at the sub-pixel level. This stringent requirement arises from the desire to preserve robust point-spread-function photometry everywhere in the field.

By modeling the flux seen by a detector illuminated by surfaces at various temperatures inside FourStar, it was concluded that maintaining the optical elements and support structures following the cold stop at 200 K was adequate to suppress thermal emission to the background-limited regime. The interior of the instrument will then contribute $\sim 5\%$ of the total thermal background under the coldest ambient conditions. Thermal emission outside the filter bands and from opaque mounting surfaces close to the detectors is suppressed by cooling the filters, field flatteners and (of course) the detector mosaic to 77 K. Components of the reimager (L3 through L6) are thus cooled to 200 K. There are three associated advantages to cooling these lenses only as much as necessary: thermal expansion effects, material stresses, and LN_2 usage are reduced.

The indices of refraction of the four infrared glasses at our operating temperatures needed to be determined. They are used in four different temperature regimes: SiO_2 at $\sim$ 285 K and 270 K (L1 and L2), CaF_2 at 200 K (L3, L5, L6), S-FTM16 at 200 K (L4), and S-TIH1 at 77 K (L7). Except for the SiO_2 window at 285 K, these temperatures deviate enough from ambient that a careful estimation of the indices of refraction at operating temperatures was necessary for input to the ray trace model. This subject is treated in Appendix A.

All lenses were obtained from Janos Technology, Inc. Transmissions greater than 99% at the band centers were realized. Table 3 lists several of their properties. The filters were manufactured by Barr Associates.

4.1. Optical Tolerancing

Prior to commencing the detailed optomechanical design, we performed an analysis of the ZEMAX spot diagrams to establish decenter, tilt, and spacing sensitivities. We also sought to establish a set of fabrication tolerances for each element, balancing manufacturing difficulty against performance degradation. The analysis was done in two steps. First, we did a sensitivity analysis to gauge the effect of each tolerance applied individually. This indicated which tolerances were stringent and which were not. Second, we did a Monte Carlo analysis which applied a random amount of error for each tolerance within the limits set for that particular tolerance. The combined effect of all tolerances was then analyzed to build meaningful statistics and to thus provide insight into the likelihood that our one system would deliver the desired optical performance. The tolerance errors considered included the optomechanical element and group decenters, tilts and spacings, and fabrication; and those of lens properties: indices of refraction, radii of curvature, surface irregularities, wedge, center thickness, and asphere decenter. In all, 144 tolerance errors were included in the analysis.

To estimate a nominal allowable performance degradation due to the optics alone, we assumed that the rms sum of all degradations *not* due to the optics, (telescope, guiding, atmosphere, pixelization) amount to $0\farcs3$ (2 pixels) FWHM images. Then a 1 pixel blur due to the optics would increase this to approximately $\sqrt{2^2 + 1^2} = 2.2$ pixels, which we deemed acceptable. This led to the condition that if we wanted the optics to deliver images with 1 pixel FWHM, then a 1 σ spot size of 7.65 μm would be acceptable. The Monte Carlo results showed that 80% of the hypothetical systems were better than this. This led to a table of element and group tolerances that the optomechanical designers and manufacturers were obliged to achieve (Table 3).

5. Optomechanical Designs and Implementations

The optomechanical designs were carried out in parallel with the thermal designs as discussed in §6, as they closely interact with each other. Both mechanical and thermal models start from the system-level vessel concept shown in Figures 1 and 6.

5.1. Vacuum Vessel

The goals of the vacuum vessel mechanical design were as follows: (1) maintain surface figure and alignment of the optics subject to rotations under gravity loading, vacuum loading, and temperature changes; (2) minimize rigid-body motions of the system as the telescope moves as these are manifested as pointing errors; (3) ensure safe stresses in the vessel under vacuum loading; (4) minimize overall weight.

The vessel was constructed of four welded 6061-T6 aluminum tubular sections plus a front flange and load ring as shown in Figure 6. Vacuum integrity is maintained by the use of (Viton) O-rings captured in trapezoidal grooves. The components of the vessel were machined and vacuum welding was by Stadco. The overall dimensions of the vessel are 3 m long, 0.83 m in diameter, and 0.80 cm in wall thickness. The load ring, of 7075[8] hard-anodized Al, has two functions: it provides support for the CM and is placed close to its center of gravity, and second, it is the large diameter surface upon which the instrument rolls. To work within the focal plane area the assembled vessel is separated at the section 2 - 3 interface. The two sections meet such that a raised boss on section 2 mates with a recessed cut on section 3. The front end and back end of the instrument are defined to be before or after the section 2 - 3 interface. Alignment of the front end and back ends is thus

[8]7075 was chosen for its yield strength; stainless steel could have served as well, but would not match the CTE of the vessel.

accomplished by having the mating diameters machined close enough that a smooth sliding fit results.

5.2. 77 K and 200 K Radiation Shields

The 77 K radiation shield is a machined tubular section 6061-T6 Al rigidly attached to the shield dewar. The end of the tube facing the CM is covered by a stiff plate which has a central hole for the light to pass through.

The 200 K shield is similarly constructed. It is suspended inside the vessel with six G10 tabs (to limit heat transfer); these are adjustable in length for alignment purposes, and couple through flexures to prevent thermally-induced stresses. At each end of the 200 K shield are baffles whose apertures match the footprint of the optical beam at those locations.

The two radiation shields are coupled thermally through three soft stranded copper braids, so the mechanical interface has no rigidity. This design allows heat to flow from the 200 K shield to the 77 K shield. These braids are clamped to the top cover of the 77 K shield when the vessel is being assembled. We refer to these braid/clamp units as the *cold clamps*.

5.3. Optics Mounts and Entrance Window Lens Assembly

The requirements adopted for all optics mounts were (1) the cell design would accommodate differential contraction between glass and metal; (2) the lenses must be placed correctly (centered and spaced), with no tilts when cold and under gravity loading; and (3) there would be no adjustments. The key mechanism adopted is that of a *roll pin flexure*,

explained by Smee (2010), and shown in Figure 7: a number (typically 12) of compliant flexures are machined into an aluminum ring, and these locate the lens radially. Because the roll pins exert only light spring loads, they easily accommodate thermal mismatches between glass and metal at any point in the cooldown. High precision Electro-Dynamic Machining (wire-EDM) guarantees very good centration. This basic design was used for all lens mounts and is shown in Figure 7.

The axial locations of all the lenses are set by seating each lens against an appropriately curved ring within the lens cell. Light forces are applied through the edges of the each lens via stacks of Belleville washers.

The window lens assembly, shown in Figure 8, incorporates two roll pin flexures, one for each of lenses L1 and L2. Each lens is located in a cell and is held in the axial direction by a retaining ring. To reduce contact forces at the cell/lens interface the cell has a contoured ledge matched to the curvature of the lens. A retaining ring clamps the lens onto the ledge; each ring maintains a precisely predicted force against its lens via a stack of Belleville washers. Each cell is screwed onto the barrel in such a way as to maintain accurate radial position of the cell. Finite Element Analysis (FEA)[9] of lens motion within their cells showed 0.076 mm for L1 and L2 and $\sim$ 0.025 mm for the other lenses for a 180° rotation.

The Window Lens Assembly weighs 45 kg, is 490 mm in diameter, and is 143 mm long. Some features of the design are: (1) the interior surfaces are painted with Lord Aeroglaze Z306 paint[10]; (2) the lens cells and the retainers are coated with a teflon-impregnated anodized coating (Tufram) to reduce friction at interfaces; and (3) a baffle is attached to

[9]All finite element analysis for this project was carried out with the ABAQUS software.

[10]See Appendix B. All parts were painted by Barry Avenue Plating.

the back side of the cell. It has aluminum foil on the window-facing side to help reduce the heat load of the window upon the interior and Z306 on the shield side to help reduce scattered light.

5.4. Camera Module (CM)

A sectional view of the CM is shown in Figure 9. Each lens is held in place with a roll pin flexure cell and retaining ring in analogy with the window lens assembly. The unit weighs 40 kg, is 300 mm in diameter, and is 650 mm long. As noted previously, it operates at 200 K. Figure 10 shows the CM being installed into vessel section 2.

A FEA model was created to evaluate contact stresses and deformation of L4, the lens most vulnerable to breakage. The loads, applied step-by-step, are due to the retaining ring fastener spring load, the roll pin flexure preload, the assembly cooldown thermal stresses, and the roll pin flexure cold load. The model showed that the lens was safe with respect to these forces, and that axial deflections at the lens center were well within the optical tolerances.

The CM is located at its center-of-gravity via three titanium flexures attached to the interior diameter of the load ring at the vessel section 1 - 2 interface. These are adjustable in tip-tilt, piston, and radially for optical alignment. The heat load through the flexures is minimized by the relatively low conductivity of titanium and a long thermal path.

5.5. Back End of the Vessel

Figures 11 and 12 illustrate assembly and sectional views of the back end of the instrument. The back end serves a number of purposes: (1) it contains the shield and

detector LN_2 dewars; (2) upon the latter are mounted the focal plane mechanisms and detectors; (3) it carries cooling power through the cold clamps from the shield dewar to the radiation shield; and (4) it provides optical baffling of the focal plane. A second handling cart is used to support the back end for transport and servicing in a cleanroom.

An aluminum support ring (not to be confused with the load ring) shown in Figure 11, is clamped between the sections with O-rings on each side to provide vacuum integrity. The support ring is so named for its function by rigidly clamping the detector dewar to the vessel wall. This is accomplished via six G10 flexure clamps. They are shaped to grab the front and back plates of the detector dewar near its edge and to carry the load out to the support ring.

Both the detector and shield dewars are made of 6061-T6 welded aluminum. The detector dewar has a usable volume of 14 liters and a hold time of five days. The shield dewar has a 30 liter usable volume and a hold time of just less than a day (depending on ambient temperature conditions). Its on-axis fill port allows for a stationary fill tube and automatic filling under computer control. The mechanical design of both dewars is the same: round, flat, weight-relieved plates form the end caps of the dewar, and the wall is a seam welded tube. The dewars are not stress relieved after welding. Four internal tubular supports spanning the gap between the end caps help prevent the dewar plates from deforming at 77 K. The fill tubes are stainless steel bellows, attached to the dewar end cap via a blast-welded aluminum/stainless junction. All welding of the dewars was done by Precision Cryogenics. Figure 13 shows the shield dewar under construction and illustrates the mounting of a cylindrical capacitive sensor for monitoring the LN_2 level (see §9.6.1).

A G10 support tube carries the load of the shield dewar to the vessel (see Figure 11). The rigidity of this support scheme is not important because the 77 shield and 200 K radiation shields are not coupled.

As is common in cryogenic vacuum systems it is important to provide a quantity of molecular sieve (getter) to trap air and molecules outgassed from within the vessel and O-rings, as well as from low-level leaks around and through O-rings (Atwood and O'Brien 2000, Danielson's reports at www.vacuumlabs.com). We employ $\sim$ 1840 cm^3 (0.9 kg) of activated charcoal located in a can screwed to the shield dewar in the gap between the shield and detector dewars (Figure 12). This choice (instead of zeolite) was made for reasons of reactivation: the charcoal needs to rise only to ambient temperature to outgas its trapped molecules.

5.6. Vessel and Detector Dewar Flexure Models

A detailed FEA model of the instrument was created to study flexure. The goals were to determine the motion of the detector under a 1 g load for a 15° rotation of the instrument. There are two contributions to the flexure: the overall bending of the vessel and translation of the detector within the vessel. In-plane motion leads to image smearing while out-of-plane motion leads to defocus. The rotation angle specification was set by the longest conceivable exposure (four minutes) as the telescope moves close to the zenith and is thus quite conservative. The vessel flexure model yielded, for the worst case of both dewars filled to capacity with LN_2 (i.e., half full), a decenter of 14 μm and a tilt of 0.8 μm top-to-bottom for the detector dewar. The half full detector dewar model translating within the vessel indicated a decenter of 16 μm and a tilt of 0.3 μm. Summing these two contributions, gives, for a 1 g gravitational change in force, a maximum image motion of 30 μm, and thus $\approx$ 7.7 μm over a 15° rotation. This is $\leq$ 0.5 pixel and is clearly quite acceptable. Defocus due to flexure is negligible.

6. System Thermal Design: Goals, Analysis, and Implementation

The objectives of the thermal design model were to predict temperatures throughout the system, estimate the heat loads and cooldown time, and thus guide the optomechanical design. As with the mechanical design, the thermal model starts from the system-level vessel concept shown in Figure 1. To review the situation, we have an inner dewar at 77 K cooling the detectors and focal plane mechanisms and a larger dewar cooling the radiation shields. To simulate cooling of the CM a model thermal resistor couples the two radiation shields. The actual resistor was to be designed so that the shield would achieve $\sim$ 200 K passively, i.e., close to the desired CM temperature. The CM would then exchange energy with the shield, mostly radiatively, during cooldown and respond very slowly to changes in the radiation shield temperature.

6.1. Thermal Modeling Strategy

The thermal design model parameters depended on the optomechanical designs and vice versa. For example, a fairly complete mechanical model for the CM had to exist before the thermal model could be completed. To solve this problem, the modeling strategy followed an iterative process whereby: (1) accurate analytical and FEA submodels for the key assemblies such as the entrance window assembly, CM, mounting flexures, etc, were developed and evaluated; (2) simplified versions of these submodels were created for use within a larger next iteration system-level design; (3) the resulting system-level temperature profiles were fed back into the heatflow paths to the submodels to adjust their detailed optomechanical/thermal designs.

The thermal model required assumptions about high and low emissivity surfaces. For those surfaces needing high emissivity, e.g., the inside and outside surfaces of the CM, and

surfaces near the focal plane, we used the properties of Z306 ($\epsilon = 0.95$; see Appendix B). An emissivity of 0.05 was assumed for aluminum foil and multi-layer mylar blankets.

The thermal properties of the lenses and barrel comprising the CM were analyzed in detail and its transient behavior was predicted. As outlined above, it was then replaced by an equivalent simple model in a system-level transient coupled radiation/conduction model of the entire inside of the vessel. The results of this analysis gave the transient temperatures and heat flows of all modeled elements in the system: the window, radiation shield, CM, and vessel. It also gave accurate thermal energy transfer properties needed for designing the thermal resistor between the two sections of the radiation shield. The model heat loads are in Table 4. Two important results were the total FouStar heat load, 72 W at 285 K ambient, and the four day timescale needed to bring the CM to 200 K.

6.2. Thermal Considerations in the Entrance Window Design

The design of the entrance window doublet (L1 and L2) was found through modeling to be very important from a thermal point of view. As is common in cryogenically cooled instruments with large entrance windows, the interior surface of the window faces a cryogenic interior and will develop axial and radial thermal gradients. The magnitude of these effects depends not only on the conductivity and emissivity of the window material and the temperature of the interior, but also on the edge mounting design. At the very beginning of the project a detailed model was created to gauge the severity of the problem for a single window. The emissivity of the window at the peak of its energy output (10 μm) was assumed to be unity. The model predicted an unacceptable central temperature depression $\sim$ 15 K below ambient. Such temperatures would lead to condensation (if not icing) at dewpoints occasionally encountered at Las Campanas. Consequently, three lens-pair models were developed, where now the back surface of L1 illuminates L2 and is

expected therefore to equilibrate at a higher temperature. The models were run for ambient temperatures of 268 K, 285 K, and 300 K. In each model the edges of both lenses were held near ambient with realistic metal/glass interface conductivities. In the nominal 285 K case the center of the exterior surface of L1 is predicted to be 279 K, i.e., 6 K below ambient. While this is a large improvement over a 15 K depression, de-humidified air must still be blown across the window.

The temperature distribution of L6 was also modeled, as it is radiatively coupled to the 77 K surfaces of the filters, filter enclosures, etc. In equilibrium, the CM and the edges of L6 are at 200 K and the center of L6 is modeled to be at 195 K. Ray tracing indicated that this should not materially affect the final image quality.

6.3. Thermal Design Implementations

The detailed designs for the actual CM, radiation shields, vessel and vessel walls, etc, were dictated by a combination of optomechanical and thermal modeling results of the various components. Throughout the interior of the instrument, aluminized mylar multi-layered blankets, aluminum foil, and aluminized plastic sheets (All-Foils foil for use in vacuum systems), were employed on surfaces requiring low emissivity[11]. These surfaces included the outside wall of the radiation shield, the inside wall of the vessel and the inside wall of the 77 K section of the radiation shield.

The conceptual and thermal designs of the radiation shields were successful: temperature measurements at four places along the 200 K shield and around the CM showed $\sim$ 200 K temperatures, later held there via temperature regulated resistor. Thus the cold clamp design was successful, i.e., no iterations were needed to control the coupling

[11]The aluminized plastic sheet has enough stiffness to be easily usable on concave surfaces.

satisfactorily. Their function as a conduit for thermal energy originating from the vessel walls and window to the LN_2 reservoir of the shield dewar was modeled correctly.

Table 4 gives the expected and measured LN_2 consumption rates. The measured rate exceeds the expected rate by $\sim 15\%$; this discrepancy is deemed acceptable in view of the idealizations of the thermal/geometric model.

Filtered and dried ambient temperature air from within the telescope system is used to help keep the entrance window dry. We have never found condensation or icing.

A final factor concerns the radial temperature gradients in L1 and L2; these do not materially affect the final image quality.

7. Mechanisms

FourStar has five internal mechanisms. Four are on the detector dewar cold plate at 77 K, and the pupil mechanism mounted on the CM barrel at 200 K. Each mechanism has a gear train driven by stepping motors exterior to the vessel, except for the detector focus which is manually operated and used only during servicing. Penetration of the vacuum walls is accomplished by Ferrotec Ferro-fluidic feedthroughs. All mechanisms employ small ball bearings (0.25-inch shafts). We used Bearingworks bearings with Dicronite races and ceramic balls, specially designed to function at cryogenic temperatures. In all cases bearing recesses were reamed larger than the bearing outside diameters to accommodate differential thermal expansion between the two materials.

7.1. Focal Plane Mechanisms - Filter and Field Flattener Wheels

Figure 14 shows an exploded view of the focal plane mechanisms and Figure 15 shows a photograph of the actual filter wheels. To provide an adequate filter capacity we implemented two filter wheels, with wells for five 94 mm square filters and one open position each. Note that the filters are located near the focal plane rather than near the pupil plane so that field-angle dependent wavelength shifts are negligible[12]. The three specially optimized field flattener lenses are mounted in their four-position wheel just forward of the focal plane. The fourth position of this wheel is occupied by the detector alignment test optic, used solely for optical alignment purposes (§8.1).

The wheels rotate on 20 mm diameter axles, using angular contact bearings. Each wheel has a gearbox using miter and spur gears to provide mechanical advantages of 6× or 12× for the two filter wheels and 8× for the focal plane wheel. These mechanical advantages are further increased by a factor of five via secondary gearboxes located outside the vessel. The combined mechanical advantages lead to an average time to change filters $\sim$ 1 minute. Internal space constraints and concerns regarding maintainability and electrical accessibility led to the concept whereby the wheel positions are externally and absolutely encoded. The three wheels are enclosed in light baffles whose internal surfaces are painted with Z306. This suppresses thermal leaks from feedthroughs and scattered radiation making it past the pupil stop, helps cool the filters and lenses, and keeps them clean.

To ensure the fixed locations of images of particulate matter or other surface irregularities (such as scratches) on the filters or lenses, each wheel is located in angle with a highly reproducible mechanical detent system. Three spring-loaded detent arms hold

[12]In addition, location of filters at the pupil plane in this design would have both awkward and expensive.

bearings (Figure 14) that roll into notches around the circumference of each wheel. The in/out locations for the arms are sensed by micro switches - two per arm for redundancy.

7.2. Focal Plane Mechanisms - Detector Module

The overall size of the instrument and the possible stack-up of tolerances led us to adopt a conservative approach to aligning the plane of the detectors orthogonal to the optical axis. The detectors require alignment in tip, tilt, and piston. The envisioned alignment procedure was an integral part of the design of the detector module. The image sizes at $f/3.6$ are quite sensitive to axial location so we wanted to be able to test and adjust the detector locations without having to remove and/or replace them (perhaps) several times. The procedure for achieving both depends on using fine adjustments in the detector module in concert with an optical alignment fixture/lens set. Figure 16 shows the module in cutaway (with one detector removed) and perspective views, and Figure 17 shows it with an open ASIC box.

Each detector is rigidly mounted on its own Titanium-Zirconium-Molybdenum (TZM) block, chosen for CTE matching to the detector packages. Each block is kinematically mounted to an inner frame via three adjustable hard points that give each detector tip-tilt-piston adjustments independently. Four access holes allow adjustment from behind the module without removing the detectors. Four load springs push the inner frame onto a focus piston hard point within the inner frame; a shaft seated against the hard point is driven via focus gears from outside the vessel. Precise axial motion of the inner frame is guaranteed by 8 stainless steel (SSTL) flexures between the frames. The outer frame is kinematically mounted to the 77 K surface of the detector dewar for overall axial location and tilt via three adjustable global hard points and clamp screws. Indium straps provide thermal coupling between different parts of the assembly. Each detector has its own 10 cm

PCB flex cable leading to its ASIC on one Cold Card. A cover plate painted with Z306 is mounted on the outer frame for baffling (not shown).

Hidden in this view are a heater resistor and temperature sensors used in a temperature servo control loop. They are clamped underneath the inner mounting frame. Two additional sensors provide redundancy. A thermal cutoff switch (Sensata/Klixon 4344 series), also clamped underneath the inner frame, will disable the heater circuit at 40 C to avoid a potentially damaging thermal event caused by failure of the servo loop.

7.3. Cold Stop and Pupil Mechanism

The cold stop blocks radiation otherwise reaching the detectors, from around the circumference and at the center of the pupil image, as is usual in infrared cameras. The stop is shown in Figures 18 and 19. Its outside diameter is adjustable so as to minimize the thermal background in K_s and maximize the throughput in the other bands. It is placed at the focus of the K_s image where the rejection of thermal emission is the most critical. A central stop, also at the K_s image, is a spider-mounted disk painted with Z306. The adjustable pupil opening is implemented with an iris; it has a pre-determined setting for the K_s bandpass, and is used wide-open for J and H. (The J-band pupil image lies 51 mm in front of the K_s image.) The drive for the iris is operated through a worm gear set with a precision potentiometer-type encoder.

8. Ancillary Optomechanical Engineering

8.1. Optics Verification and Detector Alignment Scheme

To verify the laboratory optical performance of a reimaging optical system such as FourStar one often employs extended targets such as test patterns, or point sources of light in the focal plane. This approach is problematic with Four-Star because the surface of best image quality of Magellan is both curved and aberrated in the outer field. For instance, at a radial telescope field of 16 cm, corresponding to the corner of the FourStar field, the sagitta of the best fit spherical focal surface is 5.6 mm while ray errors are approximately a factor of five greater, with respect to the center, than in the corrected re-imaged focal plane. Thus the notion that the FourStar optics simply reimage the field of the telescope focal surface is somewhat simplistic as significant flattening and image correction to the telescope field are also effected. The FourStar optical system is best understood in the context of a unified optical system of instrument plus telescope optics, i.e., a combined system, balancing optical aberrations.

To provide a reference for adjusting the individual tilts and focus shifts of the detectors, and to test overall optical alignment in the laboratory, it was decided to image an array of point sources. Even if such an array were developed on a machined fixture replicating the curved focal surface of the telescope, point sources cannot simulate the complex geometry and ray paths of the off-axis aberrated images of the telescope. To reduce this to a tractable problem, we decided to test instead a conjugate optical system, nearly identical to that of FourStar. This conjugate system was formed by adding an optical element (a special version of L7) in the fourth position of the flattener wheel. This test optic is an uncoated bi-concave (negative) CaF_2 lens, the first surface of which is aspherical and diamond-turned. It was found that by operating only in the H band, this lens could be designed so as to accurately reimage point sources confined to two concentric rings in a common focal plane

located at the vertex of the telescope focal plane position (defined as 210 mm ahead of the L1 vertex). These rings were chosen to be 5% and 95% from the center of the field towards the edge. The ray errors of the conjugate system were predicted to be less than one pixel FWHM for a correctly designed and built FourStar optical system, including of course the test optic itself. Ray errors contributed by the absence of the field flatteners break the conjugate symmetry, but these are the most tolerant elements in the design.

To generate sources in the conjugate system test focal plane, a fiber-optic plug plate fixture was constructed. It holds a locus of 24 single-mode illuminated fibers total (six per detector) arranged in the two required concentric rings. The fibers simulate point sources approximately 10 μm in diameter with an $f/4$ output fan (ensuring full pupil illumination). The results the of the tests made with this setup are presented in §12.

8.2. Stray Light Analysis

Appendix B contains a brief summary of the analysis performed by the consulting firm Photon Engineering, Inc. Three sources of unwanted radiation were modeled: ghosts, scattered/stray light, and thermal emission. In summary, (1) all ghosts were very small compared to the peak source irradiance of a point source; (2) the system as a whole was found to be well baffled; and (3) the thermal self-emission of the instrument itself is negligible.

8.3. Infrastructure Required to Operate the Instrument

The guider is provided by the telescope. There are two probes, each of which can operate either as a guide camera or as a Shack-Hartmann sensor for telescope primary mirror figure control. These cover a guide field not much larger than the footprint of the

FourStar field. The latter is so large that suitably bright Shack-Hartmann stars ($\leq$ 15th mag in R) are sometimes hard to find as they must lie within a narrow strip ($\leq 1'$ wide) on each side of the FourStar field. Palunas et al. (2010) give a detailed description of the operation and performance of the two-probe system.

The main instrument support cart is used both in the lab and on the telescope. FEA analysis was used to ensure stiffness with minimum weight.

Utilities between FourStar and the telescope are located in an IGUS chain-type cable wrap provided as part of the existing Instrument Rotator. These are minimal. From the telescope to the instrument are routed AC power, chilled glycol/water for cooling the electronic racks, DC power for operating the autofill system (§9.6.1), and dry air for blowing on the entrance window. Two fiber-optic cable pairs (1 Gb s^{-1} Ethernet; one is a spare) carry commands to all the electronic units on the instrument (including the detector computers) and carry all diagnostic information plus science data to a control computer and data reduction cluster.

9. Control and Data Acquisition System

9.1. Overall Considerations

The design of the control and data acquisition system was governed by several requirements. These included the adoption of Teledyne ASICs, system vacuum, temperature, and LN_2 level monitoring, as well as motion control. An important additional fact is that the instrument is rotating, so reducing the complexity and number of cables necessary to traverse the telescope and instrument cable wraps was highly desirable. Other engineering considerations motivating the design included the desire for redundancy, adherence to common standards, and easy maintainability.

Among the key approaches adopted was to use Ethernet and the Internet Protocol (IP) as a standard medium for communication and data transport between all devices and computers. This choice allowed flexibility and a significant simplification of the physical distribution of control elements, computers, and inter-device cabling. It also allowed a uniform and standardized approach to software development from the point of view of communication and data transport.

Apple Macintoshes and Mac OS X were selected for use as higher-level control and analysis computers. One design goal of the overall computer system was to provide a real-time automated data reduction pipeline delivering fully reduced products to visiting observers. Approximately a year before the instrument was shipped to Chile, the computational requirements for the pipeline were finalized, allowing us to make a selection of all workstation hardware. It was decided to build a Storage Area Network based computing cluster using Mac Xserve servers as the basic workstation element. Instrument control is implemented on the *Control Mac*, a computer dedicated to the instrument alone and running independently of the computationally oriented pipeline cluster. The server version of Mac OS X is deployed on all FourStar Apple workstations. Details of the FourStar SAN are presented in §11.2.

9.2. Control System: IP Network and Physical Layout

Figure 20 shows the control system layout from the highest-level viewpoint of the IP network. The components of the data system are physically distributed in four locations: rotating with the instrument, on the static Nasmyth platform, in the equipment room (a climate-controlled utility room below the observing floor of the telescope), and in the telescope control room. The physical architecture confines the cabling requirements of the electronic instrumentation to the vessel itself. This has three features: (1) it allows the

use of the existing facility guider cable wrap, obviating the need to develop and deploy a new and more complex wrap; (2) permits significantly shorter cable lengths for both sensitive analog signals and length-critical digital signals; and (3) consolidates the entire instrument to a transportable self-contained system on one handling cart. The Nasmyth Mac is physically attached to the cart so that it always travels with the instrument. The purpose of the Nasmyth Mac is twofold: it is a fully configured spare of the Control Mac, and it provides local control and data analysis tools when the Control Mac is not available, e.g., when FourStar is off the telescope for servicing.

The Control Mac and the data reduction Pipeline Cluster reside in a rack in the equipment room. The Control Mac is a client of the SAN. Data from the detector PCs is streamed to a Promise RAID-5 drive on the SAN as it is received, and simultaneously to a fast internal drive on the Control Mac. The maintenance of two online data copies is very convenient for manipulation efficiency, data security, and mid-term (several months) storage.

Data rates and system communication requirements guided the design of the link between FourStar and the equipment room. Early in the project, the data system was specified to be capable of handling data from the four Windows PCs at rate of 11 MB s^{-1} and stream this data to online storage for real-time reduction and analysis. This would allow, for instance, the continuous acquisition of data with a 1 s array clocking time, pixel-by-pixel resets, and a continuously repeated double-correlated readout sequence of reset-read-read. When the ASIC code was released by Teledyne it provided for a default array clocking time of 1.456 s, which we conservatively adopted, leading to a maximum required throughput of 7.3 MB s^{-1}, well within our specification.

To meet these criteria, two Netgear GS716T Gigabit network switches were deployed, one in the dewar electronic racks and one in the equipment room. A multimode full duplex

62.5 μm Gigabit fiber optic cable links the two switches to form a fiber backbone. This fiber backbone moves all data and control information between instrumentation in the FourStar electronic racks and the Control Mac and Pipeline Cluster. The fiber backbone traverses the guider cable wrap as well as the longer telescope cable wrap to reach the equipment room. Three additional important advantages of selecting fiber optic data transport are: Galvanic isolation provided to the readout electronics (helpful for reducing noise), elimination of potential ground loops, and mitigation of potential damage from lightning strikes which occasionally impact Las Campanas.

Figure 20 also depicts two additional components: 1) the *Observer Mac*, a Mac-mini running Apple Remote Desktop, an Apple-specific implementation of remote screen access based on the VNC protocol, and (2) the observatory LAN Ethernet link between the observer Mac in the control room, and the Control Mac.

9.3. Detector Readout Electronics

Adoption of the Teledyne ASICs afforded us a compact, high-speed, and low-noise set of readout electronics. At the same time, this approach led to certain interface requirements that impacted the overall design of the data acquisition system. The ASIC is designed to be operated in a vacuum at 77 K and cabled to within a few cms of its detector. Each ASIC connects to a JADE2[13] interface card external to the vacuum vessel. A JADE2 card provides interface glue logic from the ASIC (with its internal signal protocols) and USB 2.0. The JADE2 in turn streams data to an external computer via USB 2.0. This interface design imposes a maximum distance between each computer and its respective JADE2 card of five m, a USB 2.0 specification.

[13]JADE2 stands for [J]WST[A]SIC[D]rive[E]lectronics[2]

Figure 21 shows a detector readout block diagram and Figure 17 displays some of the mechanical aspects. In Figure 21 the four detectors are depicted as gray squares within their octagonal detector module footprint. Four 10 cm long PCB flex cables, shown in yellow, are connected to two custom PCB cards (in green), each of which holds two ASICs. (We found it favorable from a layout viewpoint to mount two ASICs per board - henceforth the Cold Cards). These cards are mounted within light-tight boxes attached to the 77 K dewar work surface. Four 38 cm flex cables connect to the Cold Cards and pass through the radiation shield to bridge the vacuum via hermetic Micro-D dual-sided feedthrough connectors. Short (2.5 cm) jumper cables link the Micro-D connectors to the four JADE2 interface cards, mounted in pairs within two blister boxes on the outside of the vessel. USB 2.0 cables connect the JADE2 cards to the four Windows PC computers in the electronic racks. The bidirectional arrows on Figure 21 indicate both clocks and control signals to the detectors, and data from the detectors. The ASICs provide biasing, amplification, and digitization of the detector signal voltages, while the JADE2 cards supply power and clocks to the ASICs. Also shown in Figure 21 is an external clock serial bus synchronization cable linking the four JADE2 cards. One JADE2 card is designated a master, while the other three derive clocks and synchronization pulses from it. FourStar uses custom JADE2 firmware requiring this cable, a design arrangement that is essential to eliminating pattern noise induced by otherwise beating clock signals. Not shown in Figure 21 are four power cables and two linear power supplies providing low-noise five volt power to the JADE2 cards. (The standard five volt power available from USB 2.0 is too noisy.)

Teledyne designed our specialized Cold Card, as well as the JADE2 connector cables. Because the ASICs operate at 77 K our Cold Card mounting scheme incorporates a GL Scientific designed clamp affixing the ASIC to the Cold Card. The thermal energy dissipated in one ASIC running at full speed is about 50 mW, which is shunted into the dewar cold plate (not toward the detector). Each signal cable running between the ambient

temperature JADE2 cards and its Cold Card has been designed to deliver no more than 70 mW, while maintaining an acceptably low total electrical resistance for all connections of $\sim$ 3.6 ohms. Our cable design was able to easily satisfy the competing electrical and thermal resistance criteria. A final hardware consideration was that the ASICs faintly emit light. On the recommendation of Teledyne, we enclosed them in light-tight boxes as shown in Figure 17.

Teledyne provides a complete firmware and communications software stack to program the ASIC, clock the detectors, acquire image frames (using key H2RG readout modes), and to stream data to customer-developed application programs. The Teledyne software stack runs under Windows XP mandating the use of Windows-based PCs at a basic level. A design choice was made to service each H2RG/ASIC/JADE2 acquisition chain with its own PC. This somewhat conservative approach was made, in consultation with Teledyne, to ensure sufficient processing power to handle the expected data rate as well as to avoid the potential complexity of employing multiple instances of the acquisition software stack.

9.4. Motion Control

FourStar requires the electronic control of four mechanisms: the two filter wheels, the field flattener wheel, and the pupil stop iris. We built a *Motor Controller* to perform all motion control tasks. The Motor Controller combines internal off-the-shelf electronic modules with custom-designed digital logic. The Motor Controller incorporates two Nyden Mac 300 multi-axis motion controllers and four drivers to control 5-phase stepper motors and provide a digital interface for their respective mechanisms' position encoding, limit, and/or detent switches. Filter and flattener wheel positions are externally encoded with simple absolute rotary encoders (of our own design) mated with their respective external (5$\times$ mechanical advantage) motor gearboxes. The absolute encoding scheme is backed up

by an incremental one: each wheel has an internal home position micro switch and the control software counts pulses to keep track of the position. A fully redundant set of micro switches and wiring paths are provided for the wheels to enhance reliability. Limits for the pupil mechanism also use micro switches.

The Motor Controller logic board drives front panel numeric display LEDs, useful for troubleshooting failures and for adjusting and calibrating the motor encoders. The availability of direct visual readout provides the possibility of manual override for the computer-based motion control. It has the additional advantage of not requiring a computer to display wheel positions when diagnosing mechanism problems. Recessed front panel switches allow maintenance personnel to immediately switch to redundant dewar-internal switches in the event of a failure.

The Nyden units are interfaced as IP devices using IP-to-RS-232 converters. Internal to the Motor Controller is an Acromag 962EN 16-bit ADC and a custom voltage reference circuit to implement the pupil mechanism potentiometer-type linear encoder. The Acromag ADC has a native integral IP interface.

9.5. Temperature control and monitoring

Temperature control and monitoring are inherent requirements of our thermal design. Two independent control loops are used to maintain the CM at 200 K and the detectors at 80 K. Lake Shore 340 temperature controllers using DT-470 silicon diode sensors are used to implement the control. All sensors are operated in four-lead mode using Lake Shore QT-36 wire throughout.

The temperature servo loop for the CM has four diodes: one for sense control and three for monitoring. Its heater element consists of three Minco film heaters wired in parallel and

glued to the barrel of the CM. Typical total power consumption required for stability is $\sim$ 15 W. Each servo loop is supervised by a software *meta-controller* as discussed in §10.5.

For the detectors, the control loop is used in two different ways. First, at the beginning of the cooldown phase, the temperature difference between the ambient detectors and the detector dewar, being filled with LN_2, causes the detectors to drop in temperature very quickly. We took a conservative approach toward this situation by controlling the cooling rate. The heater used in the loop is a Lake Shore cryogenic resistor clamped onto the inner frame holding the detectors within the detector module. Second, it was found that near 77 K the temperature of the detector mounting (inner) frame exhibited a variation of several tenths of a degree K over time scales of a few minutes, depending on how the detectors were clocked and powered, the current LN_2 fill level, and rotational orientation of the FourStar vessel. Such variations are consequences of changes in external heat load (for example from the ASICs), and thermal balance between these loads and the thermal paths to the detector dewar. The thermal paths are deliberately resistive for operation of the control loop. For purposes of electronic stability, it was deemed desirable to mitigate the temperature variation by applying a controlled and dominating heat load to the detector module (via its heater) *after* the initial cool down. We chose 80 K as the detector operating temperature and achieve a stability of $\sim \pm$ 0.01 K. Typical power consumption is 0.3 W. In addition to cryogenic temperature control, monitoring of temperatures at representative points in various important structures such as on the LN_2 tanks, radiation shields, the CM, and in the proximity of the filter and field flattener wheels was implemented. This monitoring is important for several reasons: (1) to ensure that dewar cooling or warm-up operations are proceeding as expected; (2) to determine when interior locations have reached thermal equilibrium (cold or warm) and thus when instrument operation may proceed; and (3) to provide a supplementary warning for unplanned exhaustion of LN_2. The Lake Shore 340 temperature controllers were each outfitted with 8-channel measurement modules fed by

DT-470 diodes.

Passively warming up the interior of the vessel to ambient temperature can be time-consuming. Because the detector dewar is well-shielded the unassisted warmup would take more than a week. To expedite this process we employed two Minco film heaters glued to the detector and shield dewars. A third Lake Shore 340 controller (a spare unit) is used to control this process.

9.6. Process Controller - Overview

FourStar requires implementation of several other functions: LN_2 level sensing and control, ambient temperature measurement, vacuum monitoring, and control of an ion vacuum pump. We decided to incorporate the required control, monitoring, and communication functions into one instrument based on a single board computer (SBC) using the Rabbit 3000 microprocessor. Custom firmware for the SBC was developed in C. An important consideration that motivated a single custom unit, as opposed to employing purely off-the-shelf solutions, was the space reduction advantage. The SBC, ion pump controller, and related interface circuity were built into a single standard chassis, forming the *Process Controller*. The unit provides both Ethernet and front panel keyboard/LCD based (user) interfaces. All key functions are programmable from the control system computer via the Ethernet/IP interface.

The ion pump controller is a Varian (Model 20 Diode) unit. A pressure readout voltage provided by the Varian is interfaced to the SBC for computer monitoring.

9.6.1. Liquid Nitrogen Monitoring and Control

Both LN_2 dewars have sensors to measure liquid levels. Each sensor is a large circular capacitor mounted close to the inside wall of the dewar. The sensing works because the dielectric strengths of LN_2 and gaseous N_2 are different. As the dewar rotates the liquid level maintains the same geometry with respect to the capacitor. As the LN_2 evaporates, the total capacitance changes, and this is sensed. The novel feature of the design is that the measured capacitance is independent of the dewar rotation angle. The capacitor itself is made of two copper strips held in close and constant proximity by G10 spacers. Figure 13 shows one of the capacitors during construction of the shield dewar. The sensing circuit consists of a precision digital sine-wave generator that feeds a sensing resistor in series with the dewar capacitors. A change in total capacitance and consequently a change in electrical reactance Xc = -$(2\pi fC)^{-1}$ results, where f is the frequency of the driving sine-wave. This manifests itself as a changing voltage drop across the sense resistor as a function of LN_2 level. Since this voltage drop is an AC signal at the oscillator frequency, it is fed to a peak-detector circuit which outputs a DC voltage proportional to the sense resistor peak voltage. This DC voltage is then sampled by the SBC.

The capacitance variation is small, $\approx$ 20-30 pF from tanks empty to tanks full. Measuring this small change accurately is difficult. For example, the absolute capacitance measurements vary on the order of 50 pF or more when cables between the Process Controller and sensor capacitors are rearranged. This means spurious capacitance changes, due to the cable capacitance both internal to the cable and between the cable and surrounding environment, dominate capacitance changes due to fill level. Thus, when deploying the Process Controller after a change of cable routing, or when deploying the spare process controller, it is necessary to recalibrate the measured capacitance values for the actual LN_2 fill level. This procedure is accomplished by a standard front panel

interaction with the Process Controller.

For the shield dewar, the LN_2 level sensing is used to control an autofill system. The system is typically configured to open a cryogenic solenoid valve when the LN_2 level falls below a certain percentage of full (usually 10%) and to close the valve at $\sim 90\%$ full. Power for the solenoid valve is delivered from the Process Controller. The autofill system usually operates twice per day. In the case of the detector dewar the level is monitored and manual filling is required every four days.

A key feature of the Process Controller is that it can function as a stand-alone controller, performing its task independently of any supervisory control, freeing the autofill process from any dependencies on high-level computers, data communications, or software infrastructure.

9.6.2. Vacuum Monitoring

Maintaining a vessel pressure of $\leq 10^{-5}$ Torr is essential to suppressing conductive heat flow and minimizing LN_2 boil-off rate. The capability to accurately, continuously, and automatically measure dewar pressure from atmospheric to $< 10^{-5}$ Torr, was particularly important during the development phase of FourStar. After vessel servicing or during routine operation it is important to be able to detect vacuum failures or slow leaks and to evaluate the operation and effectiveness of cryogenic (getter), turbo, and ion pumps.

The primary vacuum monitor is a Pfeiffer model PK 251, which combines a Pirani gauge with a cold cathode sensor. This unit allows a continuous range of vacuum measurement from atmospheric pressure to 5×10^{-9} Torr. The Pfeiffer output is a voltage linearly related to the logarithm of the pressure. The SBC samples this voltage and converts it to Torr for front panel and Control Mac display. The Varian ion pump is continuously

operated and together with the getter it maintains a vacuum of $\sim 5 \times 10^{-6}$ Torr.

9.6.3. Electronics Enclosure Thermal Management

Two racks mounted on the instrument contain the electronics. These include the four data acquisition PCs, the Motor Controller, the Process Controller, the Lake Shore controllers, network/data communication devices, and various power supplies. Each rack dissipates $\sim$ 300 W. In order to minimize the fraction of this heat convected into the dome, a thermal management system was developed. The racks are enclosed and insulated and fans drive the warm air within the racks around a plenum that encircles the chassis. The warm air flows through two heat exchangers that employ chilled water/glycol made available from the telescope thermal system. The performance of the system was tested in the lab and found to meet our design specification. About 30 W per rack of waste heat escapes into the dome.

Four temperature sensors are located in the two electronics enclosures. These are continuously monitored to evaluate cooling effectiveness and to provide warnings in the event of a failure. As a final safety measure for the electronics, thermal cutout switches set to shut down power to the racks above 40 C, are installed in each enclosure.

9.7. Operation of the Control and Data System at the Telescope

Observers work in a control room located adjacent to the telescope and above the equipment room. They access the Control Mac remotely using the Observer Mac. This computer provides two large LCD screens for displaying control and analysis system windows. Access to the FourStar private network is through a Cisco 515E Firewall Appliance, which provides a high degree of isolation between the FourStar private network

and the external observatory network.

Acquired images may be written to two hard disks simultaneously. The first disk is the internal disk of the Control Mac, serving as an online backup for the raw data. The second disk is the RAID array also accessed by the real time data reduction pipeline. Because of the large volume of data typically generated by FourStar ($\sim$ 50 GB per night), most users choose to archive nightly data to portable USB 2.0 hard drives. To support this, the USB 2.0 interface on the Control Mac is extended to the control room via a USB 2.0 fiber optic extender, where it is made available on a four-port USB hub. Visiting observers may thus copy data to portable drives without needing to interact directly with the rack of Mac Xservers in the equipment room.

10. Control System Software

The FourStar control system software is responsible for data acquisition, instrument control, and system monitoring. Figure 22 shows a software system overview. It consists of two programs, *StarGUI* and *StarServer*. StarGUI runs on the the Control Mac and communicates with the instrument devices, the telescope control system (TCS), and StarServer over TCP/IP. StarServer runs on each of the four Windows PCs controlling the data flow, one instance per detector.

10.1. Instrument Control: StarGUI

The StarGUI program runs on the Control Mac computer and is written in C using the Apple *Carbon* programming framework. All communication with other components is done via the Ethernet network (TCP/IP sockets) and therefore does not require any special drivers. StarGUI is the user interface for the observer; its main window shows all

the controls necessary to start an exposure or run a sequence of exposures and telescope moves (a *dither-macro*).

10.2. Camera and Data Acquisition Control

Figure 23 shows the StarGUI camera control window along with the dither-macro creator tool. The first group of controls defines the settings for an individual exposure. The exposure time can be set in multiples of 1.456 seconds (i.e., the detector clocking time coded into the ASIC). The *ReadMode* may be set to take double correlated exposures or Fowler samples (i.e., multiple endpoints; Fowler and Gatley 1990). Two gain settings have been implemented: the FullWell setting is used for broad-band imaging, while the LowNoise setting is used for low background imaging as it minimizes read noise.

The software abstracts the positions of the filter and field flattener wheels, and the variable pupil iris setting to a *FilterCombo* that automatically selects the appropriate combination of optical elements. Thus the observer need not worry about having the wrong combination of filters (or open position) in the beam. Loops (repeat exposures of up to 64) are taken by pressing the *Go* button.

The *Macro* group allows the observer to execute telescope dither or calibration scripts. The software offers a range of predefined macros that may be created with the help of a simple tool (see right-hand panel of Figure 23). The observer may choose from a number of standard patterns (e.g., dice-5 or square-9 in an intuitive notation) or may create a randomized dither pattern of a selectable size and number of positions. The latter choice is important for deep observations of sparse fields. Such observations require a dithering technique that ensures that no two visits point the telescope toward the field in exactly the same way. This is a conservative way of ensuring that detector artifacts can virtually

never combine to create a false signal once the dithered images are reregistered. The implementation works as follows: (1) generate a random set of n points with characteristic separation s within a box of width w and height h

$$\mathrm{w} = \mathrm{h} = 2 \times \mathrm{s}$$

fulfilling the following restriction for the minimum distance m between any two points :

$$\mathrm{m} > [\sqrt{2}\mathrm{s}]/\sqrt{\mathrm{n}}$$

This ensures that small separations are not possible. (2) The sequence of telescope moves in the list of random positions is now optimized so that the characteristic move is $\approx s$. This means that large moves are disfavored because they increase the time spent moving the telescope, and hence make the dither-macro inefficient, and that relatively small moves are disfavored for reasons of robust sky frame creation. This is a variant of the classic Traveling Salesman problem.

10.3. Quick-Look and Magnifier Windows

Figure 24 shows the *Quick-Look Window* with *Magnifier Window*. The larger Quick-Look window displays all four images in detector coordinates. A simplified compass rose (green circle) indicates North and East. The displayed frames may be scaled manually or automatically, and can be shown as raw images or sky-subtracted using any previous image. The *Magnifier* window allows the observer to zoom into any area on the full image to inspect the data. The Magnifier shows the minimum and maximum pixel values and calculates the average and standard deviation within a circular aperture of a selectable radius. It also calculates an estimate of the image diameter (FWHM) of an object at the cursor position.

10.4. Telescope Window with SkyMap, Airmass and Object-List Display

The *Telescope-Control* window in Figure 25 displays telescope coordinates, current airmass and sidereal time. It allows the observer to initiate small offsets, either by just moving the telescope, or coordinated offsetting where the guider is moved the same distance in the opposite direction to maintain telescope guiding.

The *SkyMap* window displays a star catalog (GSC, USNO-A, 2MASS) superimposed on the field-of-view of the four detectors. The view may be zoomed in or out. Clicking on a star displays its brightness (e.g., J, H, and K_s magnitudes from the 2MASS catalog). Each exposure taken leaves a persistent footprint of the detectors on the map. This allows the observer to visually monitor the progression of a dither-macro.

The *Airmass* window displays the change in airmass over time at the current pointing. The telescope pointing can also be set to any coordinates without moving the actual telescope, allowing the observer to predict the airmass time development of any field.

An *Object-List* window (not shown in Figure 25) can load ASCII files created by the observer in preparation for, or during, each run. Entries may be edited or created at any time. Object coordinates may be sent directly to the TCS, thus avoiding communication errors between the telescope operator and the observer.

10.5. Instrument System Monitoring and Control

The StarGUI monitors all temperatures and supervises the two temperature servo loops. During FourStar cool downs the software meta-controller adjusts the setpoint of the Lake Shore controller every minute to create a ramp with a selectable slope (in K min^{-1}). During warmups the temperature setpoints for the detector and optics are synchronously increased to ensure both reach room temperature at the same time. During regular

operations the StarGUI meta-controller maintains the detectors and CM at their proper temperatures, displays, and logs all temperature and heater power data.

Figure 26 shows FourStar's *LN2 & Sensors* window. LN_2 levels are retrieved and controlled by the Process Controller. Operator interaction can open or close the supply dewar solenoid valve, or control the valve and thus the LN_2 autofill system at programmable levels as described above.

Figure 26 also shows other monitoring tasks of StarGUI. It displays the vessel vacuum readings and the temperature readings for the electronics racks.

Finally, StarGUI uploads the current system status every 5 minutes to a computer located in Pasadena where a *cron* script updates a Web page showing plots of the most important sensor readings. The software automatically creates alerting emails if any sensor (e.g., pressure or temperature) indicates a problem. These emails are sent to the on-site observatory staff and to the FourStar team in Pasadena.

10.6. Detector Control: StarServer

Teledyne provides a Microsoft Common Object Model (COM) library that allows the detector control software - *StarServer* - to communicate with each JADE2 (and in turn with its ASIC) via the USB 2.0 interface. The COM library uses the Teledyne Hardware Abstraction Layer (HAL) software to interface with the USB port. The HAL is run either as a standalone program or under the Teledyne ASIC Integrated Development Environment (IDE) software. Unfortunately, the standalone version of the HAL cannot be controlled programmatically via the COM interface, requiring user action via a GUI. This would require the FourStar software to be started manually on all four PCs. Although somewhat awkward, we chose therefore to use the HAL included in the IDE, because the IDE may be

opened and controlled programmatically via the COM interface.

To our high-level application programs the StarServer software effectively abstracts away the complex details of the H2RG/ASIC/JADE2 hardware. This design allows the Control Mac (user level) software to simply use the network to communicate with the four StarServer programs, and does not require knowledge of any low level implementation details. The Windows PCs running StarServer also provide a data buffer to facilitate uninterrupted read sequences and store an entire loop sequence (up to 64 exposures) in RAM. This data is transferred asynchronously to the Control Mac.

11. On-line Data Reduction Hardware

11.1. Definition and Requirements

Under normal weather and K_s background conditions, the amount of raw K_s data accumulated during a night will approach 100 GB, if taken at a typical rate of four images per minute. For a several night run, writing this much raw data to mass media would require an inordinate amount of time. It was decided, therefore, to develop a pipeline to reduce the data during the night and possibly into the next day, so that the observer could leave the observatory with data reduced to final form. A second important reason for a pipeline is that it is a very useful resource for visiting astronomers who are not IR data reduction experts. It should thus increase the scientific productivity and potential of FourStar.

At the time of this writing, our online data reduction pipeline software is close to being complete. Rather than present a nearly finished pipeline, we have decided to presnt our fully functional product in a later publication. We therefore present here a description of the hardware alone.

11.2. SAN cluster

To determine the computational requirements necessary to meet our goal of timely online pipeline processing, benchmarks were performed in 2006 on general use single processor workstations using prototype versions of the pipeline software. These computers were tasked with the job of processing real observing data from NEWFIRM (Autry et al. 2003, Probst et al. 2008), a camera with similarities to FourStar. These tests indicated that a multiple processor approach with 24 cores using Xeon 2.26 GHz 64 bit processors would best meet our processing needs. To facilitate the capability to frequently and rapidly store, generate, and manipulate intermediate data products on disk, as well as the ability to easily share data products between all analysis computers, it was decided to implement a shared RAID-5 10 TB drive accessible to all pipeline workstations and the Control Mac.

The architecture implemented is shown in Figure 20, enclosed within the blue dashed-line box. It consists of a computing cluster of three Apple dual quad-core Intel Xeon 1U Mac Xserve servers deploying a Storage Area Network (SAN). SANs are networks of storage devices and computers for which the storage devices appear to member computers as being locally attached. The physical layer of the SAN uses Fibre Channel, a Gigabit speed switched network protocol used to transport disk blocks between member computers and storage elements such as our RAID drive. Fibre Channel is similar to Ethernet in that storage elements and workstations communicate through SAN switches connected by copper and/or fiber optic cables. As with Ethernet, these connections may be singly made or trunked for greater performance and fault tolerance. A SAN generically defines block data transfer protocols, but does not define a shared file system. To both build our SAN and a shared cluster file system, we employed Apple's XSan2, which requires three independent physical switched networks to implement a computing cluster. Two of these are standard Ethernets, the other a Fibre Channel network. The primary Ethernet

in our implementation is the private FourStar instrumentation network used for general communication between all workstations, computers and devices. This network is routed to external networks such as the Las Campanas LAN and the Internet through a firewall appliance. The second Ethernet is a separate network necessary to communicate *metadata* between SAN cluster members to implement the shared file system. Metadata is generically defined as data which describes data and is used by the SAN for managing file locking, space allocation, and data access authorization. The third switched network used by Xsan2 is the Fibre Channel network that transports blocks of file data between SAN members and shared mass storage elements (in our case a RAID-5 volume).

The FourStar computer cluster is physically deployed in a 42″ deep, 72″ high, open frame server rack, with standard 19″ mounting rails on the front and back. The rack contains four Xserve 1U servers, a 16 drive RAID chassis with dual fibre channel controllers, three network Gigabit IP switches, a Fibre Channel switch, a Cisco 515E Pix Firewall appliance, a 20″ LCD monitor, a rack mounted keyboard, a DVI KVM switch, a USB 2.0 fiber optic converter, and a Blu-Ray/DVD recorder. The local monitor and keyboard are useful for performing direct administrative and monitoring activities. The rack dissipates 1322 W. Its location in the air-conditioned Baade equipment room ensures a safe operating temperature.

12. Laboratory Performance Results

The instrument performance was extensively characterized in the laboratory during the development phase. Much effort was spent in software development and testing, while the motor controller, mechanisms, etc, were debugged, and various procedures for handling the vessel and its component parts were finalized. In the following we first discuss the optical testing, then the detectors.

12.1. Image Quality Using the Detector Alignment System

The optomechanical conjugate system built to align the detectors and to verify optical performance (§8.1) was used for several tests. The first was simply to observe the optics reach thermal equilibrium. The optical system did not achieve focus for at least a day after other interior structures had reached their operating temperatures (i.e., $\sim$ 6 days), verifying a predicted lag in glass cooling times. Focus curves of the imaged fiber tips were then made in 40 μm steps at the detector. Most image profiles had images of $\sim$ 1.2 pixels FWHM, which showed that the instrument optics (manufacturing), optomechanics (cells, stresses, etc), and alignment were performing as designed. The results demonstrated the image quality we should expect at the telescope in excellent seeing.

The offsets of the focus curve minima were used to determine tilt and focus corrections present between the 24 simulated star images on the detector mosaic. These corrections were applied to the adjustable detector support hard points on the next dewar thermal cycle, a process subsequently iterated to convergence during further cold tests. Rotation of the instrument through 180° showed $\sim$ 4 pixels of image motion, in line with expectation.

12.2. Gain, Read Noise, and Fowler Sampling

We used the well-known variance method to determine the gain (in e^- ADU^{-1}) on a pixel-by-pixel basis. These values were then averaged to give the gain for the entire detector. Read noise values follow from converting the noise for dark frames into e^- rms. Table 5 gives the resulting values for each detector. The measured read noise values for our LowNoise mode were close to those provided by Teledyne. Factors contributing to these satisfactory results included powering the JADE2/ASIC circuits with linear power supplies, mounting the ASICs in close proximity to the detectors, and use of the JADE2 card clock

synchronization.

Experiments in read noise reduction via Fowler sampling were carried out. Purely random noise is expected to decrease as $\sqrt{N}$, but this is never observed to be quite the case for N > 32, as other low-level noise sources begin to contribute. We found our results to be consistent with those of the Teledyne test. So far we have used this mode very little as most of our data have been strongly background-limited.

12.3. Gain Modes

Our implementation of the LowNoise and FullWell gain modes was briefly mentioned in §10.2. The internal amplifier and ADC signal chain embedded in the ASIC has a number of programmatic choices that are hidden from the observer. Sensible default choices are adopted by Teledyne for our ground-based detectors. One exception for which we permit a choice for the observer is that of amplifier gain modes. The fundamental reason for deploying two modes is because the ADCs (embedded in the ASIC), while presenting a 16-bit word for readout, actually realize only 14 bits of resolution, not 16.

To prevent this fairly coarse ADC precision from making a significant digitization noise contribution to the total read noise, in LowNoise mode, the ASIC may be configured to amplify the signal from the detector before presentation to the ADC input, to the point where the digitization error is dominated by the amplified detector-only read noise. This choice, however, forces a compromise since the 64K total count range of the ADC then spans only $\approx 9 \times 10^4$ e^-, less than typical full-well saturation values of $\approx 1.45 \times 10^5$ e^-. Nevertheless, under conditions of low background, not requiring highest well-depth, operating in the LowNoise mode can be optimal.

In the FullWell mode, the ASIC electronic signal gain is reduced from that of LowNoise

mode so that the 64K maximum ADC count range accommodates the full electron well-depth (and beyond) of the detectors. The measured read noise in this mode has a digitization noise component equivalent to $\sigma \sim 5$ e$^-$. This mode is preferable for observing scenarios that are decidedly background-limited, which is the case for most FourStar usage.

12.4. Linearity and Full Well Capacities

HgCdTe detectors have a non-linear response up to the full well level. FourStar observers are advised to operate below the point at which the linearity correction for any pixel is $< 10\%$ to ensure optimal photometry.

A sample linearity diagram for the FullWell mode is shown in Figure 27. Measured Raw and True ADC counts (the latter proportional to time for a steady light source), are plotted for a typical pixel. A fit to the data is shown with percentage fit error in the bottom panel. The fit is of the form

$$\mathrm{ADU_{true,i,j}} = \mathrm{ADU_{meas,i,j}}(1. + \mathrm{A_{i,j}} \times \mathrm{ADU^{1.5}_{meas,i,j}}) + \mathrm{B_{i,j}}$$

and follows the data well. Here the indices i, j denote an arbitrary pixel. The $\mathrm{A}_{i,j}$ coefficient for this particular fit is 1.2×10^{-8} and B = 0. The residuals from the fit are shown in the bottom panel. The equation closely follows the deviation from linearity until the deviation exceeds $\sim 1\%$. This occurs at a raw count of 43,000 ADU, corresponding to a corrected count of 48,000 ADU or 120,000 e$^-$.

The shapes of the linearity curves found for other cameras, e.g., the MOSFIRE detector (Kulas, McLean, and Steidel 2012), and our Teledyne test results, are clearly more linear up to a higher level than ours. According to Loose (2012) this is not surprising given our choice of pixel Vreset and Dsub voltages. (Our values are 0.30 and 0.60 V respectively).

12.5. Darks and Instrument Stray Light

The measured dark count is ~ 0.3 e^- s^{-1} $pixel^{-1}$, much larger than ~ 0.01 e^- s^{-1} $pixel^{-1}$ quoted by Teledyne. We believe the difference arises predominantly from light leaks within FourStar, but have not attempted to find or reduce it. This is because FourStar is fully background-limited for all filters and for all observing parameters.

12.6. Inoperable Pixels

All four detectors display inoperable pixels, mostly distributed randomly. There are also three large ($\sim$ 30 pixel) coherent inoperative clumps. Four different effects cause inoperable pixels: (1) a *dead* pixel is one in which where the Readout Integrated Circuit (ROIC) and the detector material (the HgCdTe) are not connected; (2) a resistively shunted pixel does not display a clean photodiode behavior and therefore its response to light is abnormal. This is typically caused by a processing defect; (3) a *hot* pixel exhibits a larger than average dark current. Typically they appear brighter than neighboring pixels and the effect becomes more noticeable at higher operating temperatures; and (4) an intermittent or stuck pixel jumping between discrete voltage states is sometimes referred to as a pixel with Random Telegraph Noise (RTN); this is a manufacturing defect of the ROIC (Blank 2011). The inoperable pixel counts are 0.3, 0.6, 1.7, and 1.2% of the total number of pixels for our four detectors. Fortunately none of the inoperable pixels or clumps pose any particular problem in data acquisition or reduction as they are easily removed in the dithering procedures.

13. Instrument Performance on the Telescope: Detector-Specific Parameters

Of particular interest to astronomers using FourStar is the on-telescope measured performance. The essential parameters were determined during six commissioning runs in 2011. In the following sections we describe performance measurements or characterizations of a number of features as they pertain to achieving the optimum use of FourStar.

13.1. Read Noise

For many astronomical infrared instruments, detector read noise measured at the telescope exceeds that seen in the lab. This was not the case for FourStar: read noise figures were the same as measured in the lab (Table 5). Nor did any patterns caused by ground loops, interference, etc, appear. Electrically speaking the instrument performed as designed. A key reason for this, as mentioned above, is the location of the ASICs only 10 cm from their respective detectors. Despite our expectation that the dome electrical environment would be noisier than in a laboratory, the system noise remains unaffected.

13.2. Radioactive Glasses

In addition to normal cosmic rays, the H2RG detectors are subject to particle bombardment from radioactive materials, and in particular the lenses, within the instrument. The S-TIH1 field flatteners could be important as they lie very close to the detectors (Epps 2010). The dominant contributor is Potassium, present in S-TIH1 and which contains a trace of the rare decaying isotope ^{40}K. (The S-FTM16 lens is also radioactive, but is relatively far away from the focal plane.) We have measured a total rate of only 100 events per detector (from all sources) in a typical 30 second exposure. The affected pixels are easily detected and masked in the data reduction process. The

acceptably low measured rate is largely due to the thinning of the CdZnTe substrate layer (Blank 2011).

13.3. Image Persistence

Image persistence is a well-known effect, whereby a bright object leaves an after-image decaying in time, possibly slowly, and may require more than one reset of the detector to eliminate. The effect has been studied for H2RG detectors by Figer et al. (2004) who give many details pertaining to testing JWST detectors.

We have made measurements to assess the level of persistence. We completely saturated a J= 4.5 star by exposing for 1.5 seconds and measuring the magnitudes of the after-images as the star was repositioned on the detector. The first latent image was 10.6 mag fainter than the bright star after it had faded for 16 seconds. Persistence is therefore only important for deep imaging at low background levels. If it is necessary to mitigate persistence, a persistence mask can be created, since the location of every spurious stellar image in a dither sequence is known.

13.4. Crosstalk

Electrical crosstalk in H2RG detectors has been discussed by Finger et al. (2008). The effect is that spurious positive or negative ghost images of a bright source, such as a saturated star, may appear in other readout channels, not necessarily physically close to the one containing the actual star. Figure 6 of Finger et al. shows how the effect diminishes with slower clock speed. At our pixel dwell time of 10 μsec, the integrated absolute intensity in an offending channel should be at least 7.5 magnitudes fainter than that of the actual star. We evaluated the effect in our data by deeply saturating a bright star (J= 5) against

a faint background and measuring the integrated brightness of each of the (negative-going) stellar artifacts that appeared in seven channels on either side of the one containing the physical star. The integrated (negative) flux per crosstalk image was less than that of the star by ~ 11 magnitudes. As for the case of image persistence, the solution to this problem is to generate a crosstalk mask with masked pixels at all locations corresponding to the spurious images of saturated stars in each channel.

13.5. Fringing

We observe no fringing in our images, a consequence of removal of the CdZnTe substrate from our detectors (Finger et al. 2008; Blank 2011).

14. Instrument Performance on the Telescope: Optics-specific Parameters

14.1. Filters

Table 6 lists the properties of the ten filters available in 2012. The instrument passband profiles are shown in Figure 28; these include only lenses L1 through L7 and the filters[14]. They omit the uncertain contributions of the atmosphere, telescope, and detector. The filter transmission and lens reflection loss profiles were measured and supplied by the manufacturers. Lens *absorption* data were taken from the Heraeus (fused silica; L1 and L2), Ohara (S-FTM16 and S-TIH1 lenses), and Corning (CaF_2 lenses) websites. Glass absorption has a negligible effect on the passband profiles of the lenses except longward of 2.2 μm. Averaged over the K_s bandpass the combined effect of glass absorption reduces the transmission to ~ 0.89 of its uncorrected value.

[14]The FourStar website contains the passband profile data in digital form.

Although FourStar was not specifically designed for narrow-band applications, calculations and experience have shown that narrow-band filters ($\Delta\lambda/\lambda \sim 0.01$) can be used if wavelength shifts in the converging beam are accounted for in the filter design.

Substrate removal causes H2RG detector light sensitivity at wavelengths between 0.75 and 1.0 μm. This necessitated careful blocking; filter blocking scans provided by Barr Associates assured us that neither blue nor red leaks would be a problem for the broad- or medium-band filters. The two narrow-band filters at 1.19 μm and 2.10 μm do, however, require blocking. This is accomplished by operating them in series with the $J2$ and K_s filters, respectively.

14.2. Ghosts

In order to study ghost reflections off optical elements, we deeply saturated a J= 5 star through broad- and medium-band filters. No ghosts were seen anywhere in the field to levels of $<$ a few ADU pixel^{-1} in 20 s exposures. This attests to the effectiveness of the broad-band anti-reflection (AR) coatings on the optical elements and the detectors. The narrow-band filters present more noticeable ghosts, however, because they are used in series with a second filter. For example, in the case of NB119 blocked by $J2$, the same J= 5 star produces a 1 arcmin diameter ghost approximately centered on the star. The cause is a reflection between the filters, as verified by a ZEMAX trace. The integrated flux in the ghost is $\sim$ 1% that of the star and thus its surface brightness is $\approx$ 17.5 mag arcsec^{-2}. For the occasional J = 10 mag star on a frame, a ghost at $\sim$ 22.5 mag arcsec^{-2} will be present. This is $\sim 25\times$ fainter than the NB119 sky background. We conclude that in practice ghosts are not important for any of our passbands.

14.3. Image Quality in the K_s Band

Under the very best seeing conditions during early 2011, periods extending over ~ 30 min existed when K_s image diameters $\leq 0\farcs30$ FWHM were encountered. These excellent images are actually under-sampled, showing that optically FourStar is performing well. Nevertheless, during such times small detector tilts were noticed. These were measured by taking out-of-focus frames of a stellar cluster and analyzing the images across each detector. This gave the tilts and pistons required for best alignment, i.e., the point at which the best seeing images could not be improved across the mosaic. These were implemented during a servicing event in the Las Campanas clean room and new images at the telescope were taken and analyzed. There were still residual tilts affecting the images across two of the detectors, a result that agreed with simple checks using IRAF. The effect upon the image diameters is small: the change in image diameter across the latter frames was ~ 0.5 pixels FWHM across the mosaic. We have concluded that while good, the laboratory detector alignment system was not adequate to achieving precise detector coplanarity, probably because only six points of light are illuminating each detector. We plan to make another iteration of tilt adjustments during the next servicing event.

We note that the FourStar/telescope system displays some astigmatism, as can be easily seen from focus sequences on stars under good seeing conditions ($\leq 0\farcs55$ FWHM). Astigmatism was not seen in our laboratory tests, i.e., the axis of the astigmatic image does not rotate with FourStar, implying that the telescope is slightly astigmatic. We are investigating this further.

We briefly explore what the best K_s imaging performance can tell us about our instrument and conditions at Las Campanas. The telescope alone should deliver $0\farcs11$ FWHM images when the optical system is aligned and the shape of the primary mirror figure is optimal (Johns 2006). From laboratory measurements FourStar alone should

deliver 0.″19 FWHM image diameters. The contribution of guiding errors is uncertain. For the best observed 0.″30 FWHM image diameters guiding errors cannot be important so we assign them a nominal 0.″05 FWHM. Combination of the contributions in quadrature - the simplest possible method - indicates at its best the atmosphere is contributing 0.″20 FWHM to the K_s images, equal to that of the instrument. This agreement is consistent with the instrument design goals. To the extent that the telescope has aberrations, the atmospheric contribution derived above may be even smaller. To summarize the practical implications, for observations conducted in median seeing conditions with a delivered image quality of 0.″50 FWHM, FourStar is increasing the PSF from 0.″46 FWHM at the telescope focal plane to 0.″50 FWHM at the detector.

14.4. Performance: Throughputs, Zeropoints, Backgrounds, and Measured Depths

This section summarizes information pertaining to several performance parameters of FourStar. All the relevant data are contained in Table 7.

Throughput: We first discuss two kinds of throughput, *measured* and *predicted*. The *measured* throughput is defined to be the ratio of electrons detected at the output of the signal chain per photon into the telescope entrance pupil displaced to the top of the atmosphere. This requires the electronic gain in e^- ADU^{-1}, a photometric measurement of a stellar flux standard, the filter bandwidth, and a correction for the atmosphere. The *predicted* throughput combines factors relating to the transmission of the telescope, optics, and filters, and the detector QE. Table 7 lists our best estimates of the transmission and QE factors we believe characterize FourStar and the telescope. We estimate that the atmosphere and telescope transmissions are uncertain by ± 5%, and the transmission optics transmission factors by ± 2%. Because the uncertainties are dominated by those of the

telescope and atmosphere, we have not listed our individual estimates of the others. Given the uncertainties, the predicted and measured throughputs agree quite well.

The overall system throughputs as a function of wavelength are useful for convolving energy distributions of, for example, model galaxies or stars, in order to predict photometric magnitudes and colors. The FourStar website profile data do not include the roughly flat scaling factors for the telescope mirrors and detector, nor an atmospheric transmission correction.

Zeropoints: The zeropoints are given in Vega and AB (Oke 1974) mags: these are the magnitudes of a star giving one e^- s^{-1} at the output of the detector electronics. These were measured from several observations of HST white dwarf standards (see the FourStar website).

Backgrounds: Table 7 collects our measured background values at an airmass of 1.4. The J sky brightness is variable and strongly dependent on angle away from a bright Moon; see the FourStar website. The H sky brightness is highly variable, and will account for a range of several tenths of a magnitude depending on the night, and even during the time of night.

The K_s background is more difficult to study as the total thermal emission depends on the state of the telescope mirrors (surface dust, time since coating), the ambient temperature, the sky temperature, and the effectiveness of the cold pupil stop. Table 7 gives a median value of 13.3 mag arcsec^{-2} at an ambient temperature of 14 C, and 13.6 mag arcsec^{-2} at 5.5 C.

Depths: For almost any target brightness, what astronomers need most in order to design their programs are actual measured depths for nominal seeing and background conditions and assumed aperture sizes. We have begun to collect the required data; Table 7

presents the results. (See also the exposure time calculator on the FourStar website.) The depths in this table attest to the excellent median image quality and zeropoints for the site/telescope/instrument combination.

14.5. Comparison of Measured and Predicted K_s Backgrounds

We now compare the measured K_s background to that predicted in the stray light analysis (§8.2 and Appendix B). The analysis predicts a K_s background of 1143 photons s^{-1} from the instrument and telescope at 285 K, allowing for no sky emission. This corresponds to 14.16 mag arcsec^{-2}. We carried out a tipping measurement (background versus airmass), to separate the telescope plus instrument and sky backgrounds. This gave a telescope plus instrument background of 13.96 mag arcsec^{-2} at 278 K or $\sim$ 13.57 mag arcsec^{-2} at 285 K. This result, brighter by $\sim$ 0.6 mag arcsec^{-2} than the analysis prediction, leads to the conclusion that FourStar/Magellan may have excess thermal background. One important (and unfortunate) assumption made in the analysis, however, was that the emissivity in the K_s band is 0.02 for each telescope mirror, a value that is optimistic for an actual telescope. Correcting to a more appropriate reflectivity (0.95; Ridgway 2004) and allowing for some dust on the primary and tertiary, reasonable agreement between the predicted and observed backgrounds is found.

14.6. On-Sky Efficiency

We define on-sky efficiency as accumulated exposure time divided by total elapsed time for a given observation sequence. Inefficiencies arise from four sources: (1) the inherent nature of the way the detectors are read out; this adds a penalty at the beginning and end of every frame, increasing with Fowler endpoint reads; (2) data transfer overheads; (3)

telescope dithering and inefficiencies in reacquiring a guide star after a telescope move; and (4) delays necessary for occasional Shack-Hartman measurements and subsequent telescope primary mirror adjustments (Palunas et al. 2010). There are complex tradeoffs in defining observing sequences so as to maximize efficiency. The inefficiencies argue for longer exposure times and/or number of exposures taken at a given position wherein the next exposure can be started while the prior one is being transferred. When the sky background is relatively high, e.g., when OH emission causes excess H background, or warm temperatures raise the K_s background, shorter exposures must be used to avoid non-linearity effects, and this necessitates multiple frames at the same pointing. This conflicts with the desirability of obtaining many frames at different dither positions, but is sometimes necessary. For deep exposures we have measured an on-sky efficiency as high as 88% and an average of around 70%. For observations requiring many filter changes, short integration times, etc, our efficiency drops toward 50%.

15. Early Science Results

As of May 2012, 12 science programs are underway with FourStar, with five having resulted in publications (Spitler et al. 2012; Luhman et al. 2012; Lee et al. 2012; Gladders et al. 2012; Tinney, et al. 2012). One of the early motivations for building FourStar was to carry out deep surveys. Figure 29, shows sample K_s images from our Z-FOURGE program (first results in Spitler et al. 2012), a medium-band deep survey of legacy fields (COSMOS; Scoville et al. 2007, CDFS, and UDS). The image shows three 20σ galaxy overdensities at z $\approx$ 2.2. The image demonstrates the depth of our survey, and how it identifies high redshift mature clusters.

Figure 30 shows a two-color composite JK_s image of NGC 6583. This image was obtained as part of the Carnegie Hubble Program (Freedman et al. 2012), a project to

measure the Hubble constant to high accuracy using Cepheids.

Figure 31 shows a narrow-band NB210 image compared to that of a K_s image, appropriately scaled in intensity. These images were analyzed as part of the survey of Lee et al. (2012) in the COSMOS field. The three objects with cyan circles are galaxies having a significant ($> 3\sigma$) NB210 excess. They are Hα emitters at z = 2.2, confirmed through a second narrow-band excess in the NB119 filter, due to the [OII]λ3727 doublet shifted into the bandpass. Star formation rates on the order of the activity of present day Milky Way-type galaxies at intermediate redshift are being probed with these images; these three Hα emitters have observed star formation rates between 5 and 7 $M_\odot$ yr^{-1}. However, the specific star formation rates (SFR per unit stellar mass) are considerably higher than typical local spiral galaxies, as indicated by Hα equivalent widths between 150 and 300 Å (five to ten times larger than the local average of 30 Å; Lee et al. 2007).

The object marked by the dark blue circle also shows a galaxy with a NB210 excess, but in this case the responsible emission line cannot be determined. Spectroscopic follow-up will be required to determine the nature of this galaxy, as it is likely to be in the foreground with z $\approx$ 0.4.

Acknowledgements

Many people have contributed to the success of FourStar. We are grateful to Markus Loose, Richard Blank, Mark Farris, James Garnett, Jim Beletic, Raphael Ricardo, and Jing Chen of Teledyne for invaluable help at several stages of the HAWAII-2RG deployment. Our support people in Pasadena helped us throughout the project: Jeanette Stone, Sharon Kelly, Silvia Hutchison, Earl Harris, Scott Rubel, Steve Wilson, Greg Ortiz, Robbie Pitts, and machinists Jerson Castillo, Robert Storts, and Vince Kowal. We also wish to thank Charlie Hull.

A critical design review and a pre-ship review took place during the course of this project. We are grateful to Keith Matthews, Tom O'Brien, James Larkin, Rob Simcoe, Ron Probst, Jeff Crane, and Brian McLeod for their wise comments.

The crew at Las Campanas gave expert assistance during and after commissioning: Miguel Roth, Frank Perez, Povilas Palunas, Dave Osip, Mark Phillips, Marc Leroy, Glenn Eychaner, Juan Gallardo, Jorge Bravo, and many others there.

During commissioning and early science observing we benefited greatly from our collaborations with Ivo Labbe, Lee Spitler, and Janice Lee.

The funding for FourStar was largely due to the National Science Foundation (AST-0138278), and the Carnegie Institution of Washington. The Monnell Foundation provided further support. We especially thank our Director Wendy Freedman for her long-standing support. Our colleagues Pieter van Dokkum, Casey Papovich, Kim-Vy Tran, Chris Tinney, and Adam Burgasser purchased filters for the instrument.

16. Appendix A. Cryogenic Indices of Refraction for the Glasses Used

The indices of refraction for CaF_2 were calculated by applying the temperature-dependent refractive index model of Tropf (1995). This model adds temperature-dependent terms to the common Sellmeier (1871) dispersion formula and successfully reproduces the measured temperature-dependent dispersion for CaF_2 (among other materials). The Tropf input data for CaF_2 were taken from the robust set of CaF_2 measurements for temperatures from 93 K to 473 K, and wavelengths of 0.46 to 3.39 μm of Feldman et al. (1978).

To estimate the S-FTM16 indices at low temperatures, we applied the Tropf model using refractive indices and dn/dT values taken from the glass manufacturer (Ohara), which at the time were available only to $\lambda = 1.014$ μm and T = 233 K. This is somewhat above our operating temperature for the CM of 200 K and short of all our operating wavelengths except for the Y filter. The resulting Tropf fit indicated a very similar functional dependence of dn/dT vs. λ as for CaF_2, displaying what appeared to be the beginning of a shallow minimum at 1 μm (Tropf, Figure 3). The Tropf dn/dT vs. λ plot for CaF_2 at various temperatures is nearly symmetric and double-valued about 1 μm. To extend our Tropf fit for S-FTM16 further into the near infrared we extrapolated our data set to synthesize n and dn/dT values to 3.3 μm such that the resulting plots of dn/dT would also be symmetric and double-valued about 1 μm. At the time we finalized the FourStar optical design we received a private communication (Fabricant 2004) with a preliminary determination of the absolute index of refraction temperature dependence of S-FTM16 valid between wavelengths of 0.6 and 2.5 μm and temperatures between 77 K and 298 K of

$$\left\langle \frac{dn_{abs}}{dT} \right\rangle = -2.4 \pm 0.3 \times 10^{-6} \text{ K}^{-1}$$

This result, together with measurement details was subsequently published (Brown, Epps, and Fabricant 2004). To compare indices calculated with the Fabricant results to the

Tropf-based model, we converted this temperature coefficient to the more commonly used relative index of refraction as follows:

$$n = \frac{n_{abs}}{n_{air}}$$

Differentiating yields

$$\frac{dn}{dT} = \frac{1}{n_{air}}\frac{dn_{abs}}{dT} - \frac{n_{abs}}{n_{air}^2}\frac{dn_{air}}{dT}$$

Taking $n_{air} \approx 1$ this simplifies to

$$\frac{dn}{dT} \approx \frac{dn_{abs}}{dT} - n_{abs}\frac{dn_{air}}{dT}$$

Taking $n_{abs} \approx 1.57$ for S-FTM16, $dn_{air}/dT \approx -1.1 \times 10^{-6}$ K^{-1} at room temperature, and substituting the Fabricant result yields $dn/dT \approx -0.67 \pm 0.3 \times 10^{-6}$ K^{-1}.

Our Tropf model gives dn/dT from -0.6 to -1.2 $\times$ 10^{-6} K^{-1} with a mean of about -0.9 $\times$ 10^{-6} K^{-1} between wavelengths of 0.6 - 2.5 μm at 200 K. These temperature coefficients are close considering the approximations made, and in fact applying the Fabricant coefficient to Ohara index data at room temperature and extrapolating to our operating temperature (200K) resulted in negligible differences in calculated spot sizes from ZEMAX compared to our Tropf model-derived values.

The Fabricant result at the time was preliminary and was somewhat surprising (to us) due to its temperature and wavelength independence. Our Tropf model had also been used successfully to design the optics for the PANIC infrared camera which produced fully seeing-limited results on the Magellan Baade telescope (Martini et al. 2004). These factors led us to adopt our modified Tropf fit for the index values of S-FTM16.

Our original optical design called for the Ohara glass PBH-1 for the field flatteners (L7). This glass had become unavailable at the time we ordered the optics and the Ohara glass S-TIH1 was recommended as a close substitute. A simple extrapolation

of the Ohara S-TIH1 room temperature index data to our operating wavelengths and temperatures, assuming the Ohara dn/dT value given at 243 K and 0.64 μm, was made. This latter assumption also presumed a flattening of the dn/dT curve of S-T1H1 as a function of wavelength in the near infrared. No significant change in the traced spot sizes from that of PBH-1 as estimated from the Tropf model was indicated by substituting approximately-estimated indices so we adopted the PBH-1 values.

For the SiO_2 front window and succeeding element (L1 and L2), indices of refraction at 293 K were taken from the Infrared and Electro-Optical Systems Handbook Volume III and extrapolated to our operating temperatures of 285 K and 270 K using dn/dT values measured between 299 K and 471 K from the American Institute of Physics Handbook. Note that the temperature dependence of SiO_2 is a weak function of temperature and wavelength in the near infrared and almost any set of reasonable assumptions with regards to the estimation of index and index temperature dependence led to negligible differences in traced spot sizes.

A comprehensive knowledge of the index of refraction character of many infrared glasses at low temperatures based on actual measurements remains a persistent problem for the design of cryogenic infrared optical systems. This problem is exacerbated by the fact that there may also be melt dependencies for certain infrared materials. While some unsatisfactory choices were made out of necessity, our estimates were validated by the seeing-limited images realized at the telescope. This is probably due in part to the fact that much of the optical power in the system resides in the three CaF_2 elements, which have the best measured and modeled indices of the four glasses.

17. Appendix B. Ghost, Stray Light, and Thermal Background Analysis

An independent stray light analysis was contracted to and performed by Photon Engineering Inc. Three sources of unwanted radiation were modeled: ghost reflections from lenses, scattered/stray light from the instrument itself and instrument plus telescope, and thermal emission from within the camera and telescope. The geometric model of the telescope was taken from as-built drawings and included only mirrors and major support structures: the primary mirror cell, secondary support structure, and tertiary mirror turret. The geometric instrument model was taken from detailed assembly drawings, and in some cases from already built hardware near the focal plane. It included the lenses, cells, and baffles described in the text. The model incorporates simple surfaces without complicated features unless they are close to the optical beam path. The optics were modeled with absorption and reflectivities included, and very importantly the detectors were modeled with a reflectivity of 8%. (In retrospect, this assumption was pessimistic, as the detectors have a broad-band AR coating.) All interior surfaces are painted with Z306 paint[15] and there are beam fitting apertures at the ends of the baffle tube. The pupil mask is critical for proper baffling at K_s and is also at 200 K. The filter and field flattener wheels are mounted inside enclosures at 77 K, with beam fitting apertures at several places close to the edge of the optical path.

The detailed, quantitative results of the ghost analysis can be summarized as follows: (1) for point sources, the peak ghost irradiance is reduced from the peak source irradiance by at least six orders of magnitude; (2) point source ghost images contribute negligibly to the total power at the focal plane; (3) In terms of total power, the strongest ghost is the

[15]Measurements of several readily available candidate surface preparations were carried out by Photon Engineering; Lord Aeroglaze Z306, with an emissivity of 95%, was by far the best over our wavelength range of interest.

bounce path between the detector and the front surface of the band pass filter; and (4) for flat fields, the peak ghost image irradiance is 1% of the average direct irradiance.

The stray light analysis was carried out as follows: (1) a raytrace, reversed in direction from the usual case, was originated at the detector and used to identify critical opto-mechanical surfaces which can be illuminated by the detector; (2) opto-mechanical surfaces which can be illuminated directly by the 2π sr outside the telescope were identified; (3) scatter models were assigned to surfaces which appear on both lists; these are surfaces which can scatter light onto the detector in a single scatter event; (4) a raytrace was run to calculate the Point Source Transmittance (PST), the ratio between detected power and incident power. The main conclusion is that for the whole system the PST was found to be typical of a well-baffled system. In addition it was determined that the most significant scatter mechanism is from particulate contamination on the optical surfaces themselves, and that surface treatments on the interior of the instrument assembly, in particular inside the CM, are not critical to maintaining performance.

The thermal self-emission calculation follows from the instrument plus telescope raytrace. The power incident on the detector over a given wavelength band is the accumulated sum over all surfaces. The code keeps track of all transmissions, etc. The final result, for an ambient temperature of 285 K is that in the K_s band we should expect 1143 photons s^{-1} $pixel^{-1}$. Of this, 451 are due to the telescope structure, 510 due to the telescope mirrors, ten due to the instrument opto-mechanics, and 170 due to the instrument optics.

18. References

Atwood, B. and O'Brien, T. P. 2000 Further Developments in Scientific Optical Imaging, proceedings of the International Conference on Scientific Optical Imaging held in

Georgetown, Grand Cayman on 2-5 December, 1998. Edited by M. Bonner Denton. Cambridge: Royal Society of Chemistry, 2000, p.176

American Institute of Physics Handbook, Third Edition, ed. AIP and Dwight E. Gray, 1972

Autry, R. G., et al. 2003, Proc. SPIE, 4841, 525

Beletic, J. W., et al. 2008, Proc. SPIE, 7021, 13

Bertin, E. and Arnouts, S. 1996, A&AS, 117, 393

Blank, R., et al. 2011, ASPC, 437, 383

Blank, R. 2011, private communication

Brown, W. R., Epps, H. W., and Fabricant, D. G. 2004, PASP, 116, 833

Chui, C. K. 1992, An Introduction to Wavelets, San Diego: Academic Press

Epps, H. 2010, private communication

Fabricant, D. G. 2004, private communication

Feldman, A., Horowitz, D., Waxler, R., Dodge, M. 1978. NBS Technical Note 993: Optical Materials Characterization

Figer, D. F. 2004, Proc. SPIE, 5167, 270

Finger, G., et al. 2008, Proc. SPIE, 7021, 20

Fowler, A., and Gatley, I. 1990, ApJ, 353, L33

Freedman, W. L., et al. 2011, AJ, 142, 192

Gladders, M., et al. 2012, arXiv:1202.5269

Johns, M. 2006, private communication

Kulas, K., McLean, I. S., and Steidel, C. C. 2012, arXiv:1208.0314

Lee, J., et al. 2007, ApJ 671, L113

Lee, J., et al. 2012, arXiv:1205.0017

Loose, M., et al. 2003a, Proc. SPIE, 4841, 782

Loose, M., et al. 2003b, Proc. SPIE, 4850, 867

Loose, M., et al. 2006, Proc. SPIE, 6265, 77

Loose, M., et al. 2007, Proc. SPIE, 6690, 10

Luhman, K., et al. 2012, ApJ, 744, L135

Martini, P., et al. 2004, Proc. SPIE, 5492, 1653

Matthews, K. 2011, private communication

Oke, J. B. 1974, ApJS, 27, 21

Palunas, P., et al. 2010, SPIE 7733, 44

Persson, S. E., et al. 2008, Proc. SPIE, 7014, 95

Probst, R., et al. 2008, Proc. SPIE, 7014, 93

Ridgway, S. T., Chara Report at www.chara.gsu.edu/CHARA/Reports/tr91.pdf

Scoville, N., et al. 2007, ApJS 172, 1

Sellmeier, W. 1871, Annalen der Physik und Chemie, 219, 272

Smee, S. A. 2010, Proc. SPIE, 7739, 119

Spitler, L., et al. 2012, ApJ, 148, L21

The Infrared Handbook, ed. Wolfe, W. L., and Zisis, G. J. 1985

The Infrared and Electro-Optical Systems Handbook Volume III, ed. Rogatto, W. D., Accetta, J. S., and Shumaker, D. L. 1993

Tinney, C. G., et al. 2012, ApJ, 759, 60

Tokunaga, A. T. and Vacca, W. D. 2005a, PASP, 117, 421

Tokunaga, A. T. and Vacca, W. D. 2005b, PASP, 117, 1459

Tropf, W. 1995, Optical Engineering, 34, 5, 1369

van Dokkum, P. G., et al. 2009, PASP, 121, 2

Table 1. Detector and Camera Parameters

Detectors		Camera	
Parameter	Value or ID	Parameter	Value or ID
Manufacturer	Teledyne Scientific & Imaging	Number of detectors	4
Type	HAWAII-2RG HgCdTe	Electronics	SIDECAR ASICs
Channels	32	Frame clocking time	1.456 s
Pixel pitch	18 μm	Pixel scale on sky	$0\farcs159$ pixel^{-1}
Format	2048 × 2048	Format on sky	$10\farcm8 \times 10\farcm8$
Gap between arrays	150 pixels = $24''$	Number of lenses	7
Spectral Response	0.85-2.5μm	Filters	Y, J, H, K_s; 10 total

Table 2. Manufacturers/Suppliers Referenced in the Text

Company	Location	Website (www.)
ABAQUS (Simulia)	Providence, RI	simulia.com
Acromag	Wixom, MI	acromag.com
All Foils Inc.	Strongsville, OH	allfoils.com
Apple	Cupertino, CA	apple.com
Barr Associates	Westford, MA	materion.com
Barry Avenue Plating	Los Angeles, CA	barryavenueplating.com
Bearingworks	Palm Desert, CA	bearingworks.com
Brocade	San Jose, CA	brocade.com
Brunson	Kansas City, MO	brunson.us
Cisco	San Jose, CA	cisco.com
Corning	Corning, NY	corning.com
Dicronite	Santa Clara, CA	dicronite.com
Ferrotec	Singapore	ferrotec.com
GL Scientific	Honolulu, HI	glscientific.com
Heraeus	Hanau, Germany	heraeus.com
IGUS	East Providence, RI	igus.com
IR Labs	Tucson, AZ	infraredlaboratories.com
Janos Technology Inc.	Keene, NH	janostech.com
Lake Shore Cryotronics Inc.	Westerville, OH	lakeshore.com
Lord	Cary, NC	lord.com
Minco	Minneapolis, MN	minco.com

Table 2—Continued

Company	Location	Website (www.)
Netgear	San Jose, CA	netgear.com
Nyden Corp.	San Jose, CA	nyden.com
Ohara Corp.	Rancho Santa Margarita, CA	oharacorp.com
Pfeiffer Vacuum Technology	Nashua, NH	pfeiffer-vacuum.com
Photon Engineering Inc.	Tucson, AZ	photonengr.com
Precision Cryogenics	Indianapolis, IN	precisioncryo.com
Promise Technology, Inc.	Milpitas, CA	promise.com
Rabbit	Minnetonka, MN	digi.com
Sensata		sensata.com
Stadco	Los Angeles, CA	stadco.com
Teledyne Scientific and Imaging	Thousand Oaks, CA	teledyne-si.com
Varian Inc.	Santa Clara, CA	agilent.com
ZEMAX (Radiant ZEMAX LLC)	Bellevue, WA	zemax.com

Table 3. Optical Prescription and Tolerances

Lens	Dia [in]	R_1 [in]	R_2 [in]	Thickness [in]	Glass	Lsep[1] [in]	Mass [lbs]	Tilt[2] [in]	Decenter [in]	Axial [in]
L1	15.000	149.8304	-60.9100	2.1350	SiO_2	0.1969	25.5	0.0020	0.0020	0.0200
L2	15.000	49.8893	-658.9910	1.5875	SiO_2	56.7710	18.0	0.0020	0.0020	0.0030
L3[3]	6.750	31.3859	-9.0799	1.1695	CaF_2	0.3956	3.1	0.0010	0.0015	0.0030
L4	6.875	-8.3039	-30.3055	0.3976	S-FTM16	3.4122	2.3	0.0010	0.0015	0.0030
L5	8.125	-59.3446	-10.4735	1.3697	CaF_2	15.9710	6.2	0.0014	0.0020	0.0030
L6	8.125	9.3805	-57.4267	1.5792	CaF_2	7.0440[4]	6.2	0.0014	0.0020	0.0030
L7(J)	4.750	-8.5178	25.0614	0.3184	S-TIH1	0.5104	1.5	0.0050	0.0050	0.020
L7(H)	4.750	-8.6643	23.6625	0.3189	S-TIH1	0.5104	1.5	0.0050	0.0050	0.020
L7(K)	4.750	-8.8428	22.3108	0.3184	S-TIH1	0.5104	1.5	0.0050	0.0050	0.020
L1-L2[5]								0.015	0.02	0.02
L3-L6[5]								0.010	0.02	0.02
FourStar								0.020	0.04	0.25[6]

[1]The axial distance to the next element on the list. In the case of L7 it is the distance to the detector focal plane.

[2]The tilt tolerance is across the full diameter of the part with respect to the optical axis. It is tolerancing the perpendicularity of the mounting surface in the cell itself.

[3]The first surface of L3 is an even-asphere. The sagitta z of the lens surface with respect to a plane tangent to the vertex of L3 at radial distance r from the optical axis is given by:

$$z = \frac{cr^2}{1+\sqrt{1-(1+k)c^2r^2}} + \sum_{m=1}^{8} \alpha_m r^{2m}$$

Here c is the curvature R_1^{-1} for L3, k the conic constant (k = 0 our case), and all dimensions are in inches. The coefficients α are:

$$\alpha_1 = -5.1338868 \times 10^{-6}; \alpha_2 = -1.0632165 \times 10^{-4}; \alpha_3 = -3.7232482 \times 10^{-7}; \alpha_4 = 6.5760351 \times 10^{-9};$$

$$\alpha_5 = 1.9161243 \times 10^{-9}; \alpha_6 = -1.6290166 \times 10^{-10}; \alpha_7 = -5.6964442 \times 10^{-11}; \alpha_8 = 5.9003523 \times 10^{-12}$$

[4]Here shown for the J-band which includes the filter thickness. This distance changes slightly as the L7 thicknesses vary in each bandpass.

[5]Tolerances with respect to focal plane.

[6]Range in Telescope Focus.

Table 4. Heat Loads at 285 K Ambient

Source	Load (W)
Vessel Wall Radiation	33.6
Window Radiation	12.6
Shield Dewar Mounting	1.6
Detector Dewar Mounts	3.4
Cameral Module Mounts	2.7
CM Heat Input	14.2
Drive Shafts and Fill Tubes	2.3
Detector Heater	0.3
Wires	1.2
Total Heat Load	71.9
LN_2 Burn Rate Predicted[1]	1.6
LN_2 Burn Rate Measured[1]	1.8

[1]Liter hr^{-1}

Table 5. Detector Specific Characteristics

Parameter	Det 1	Det 2	Det 3	Det 4
Teledyne Serial Number	192	204	209	216
Well Depth[1] (e^-)	155,000	143,000	143,000	136,000
Depth for 10% Correction[2] (e^-)	120,000	110,000	110,000	105,000
Gain[3] (e^- ADU^{-1})	2.65	2.59	2.51	2.49
Read Noise[4] (e^- rms)	25.5	22.1	20.5	18.9
Gain[5] (e^- ADU^{-1})	1.38	1.34	1.30	1.29
Read Noise[6] (e^- rms)	19.4	16.7	16.2	15.1

[1]Saturation value.

[2]Linearity correction will be $< 10\%$.

[3]Gain for the FullWell mode.

[4]Readnoise for the FullWell mode (measured for one correlated double sample (CDS) read).

[5]Gain for the LowNoise mode.

[6]Readnoise for the LowNoise mode, on the telescope; see §13.1

Table 6. Filters[1]

Filter	λ(mean)	λ(cut-on)	λ(cut-off)	$\Delta\lambda$	λ(iso-Vega)[2]
Y[3]	1.055	1.005	1.104	0.099	1.062
J	1.242	1.126	1.354	0.228	1.240
H	1.619	1.476	1.760	0.284	1.634
K_s	2.148	1.985	2.317	0.332	2.145
$J2$	1.145	1.076	1.212	0.136	1.148
$J3$	1.288	1.218	1.358	0.140	1.290
Hs	1.553	1.474	1.632	0.158	1.575
Hl	1.704	1.626	1.782	0.156	1.71
NB119	1.1918	1.1840	1.1977	0.0137	1.1909
NB210	2.0995	2.0884	2.1095	0.0211	2.0989

[1]All wavelengths in μm.

[2]For a definition of λ(iso) see Tokunaga and Vacca (2005a). For a Vega-like energy distribution.

[3]The Y band is approximately the same as the $J1$ filter of van Dokkum et al. (2009).

Table 7. System Performance - Predicted and Measured

Element	Y	J	H	K_s
Wavelength (μm)	1.05	1.25	1.65	2.16
$\Delta\lambda(\mu$m)	0.099	0.228	0.283	0.332
Flux (Jy) for zeroth (Vega) mag	1959	1560	1050	670
Transmissions: Atmosphere	0.96	0.83	0.94	0.92
Telescope	0.78	0.82	0.84	0.85
Camera (L1 - L6)	0.902	0.890	0.899	0.863
L7	0.978	0.994	0.987	0.957
Filter	0.87	0.91	0.94	0.90
Detector QE	0.90	0.90	0.85	0.85
Throughput predicted	0.52	0.59	0.60	0.54
Throughput measured	0.49	0.53	0.63	0.58
(AB - Vega) (mag)	0.69	0.92	1.36	1.85
Zeropoint (Vega mag)[1]	26.6	26.9	26.8	26.0
Zeropoint (AB mag)	27.3	27.80	28.1	27.9
Background (e^- s^{-1} $pixel^{-1}$)	200	850	3630	3100
Background (Vega mag $arcsec^{-2}$)[2]	16.9	15.6	13.9	13.2
Background (AB mag $arcsec^{-2}$)	17.6	16.5	15.3	15.1
Depth (Vega mag)[3]	24.7	24.4	23.5	22.7
Depth (AB mag)	25.4	25.3	24.8	24.6

[1]This zeropoint is the Vega magnitude of a source giving 1 e^- s^{-1} total.

[2]At an ambient temperature of 14 C and high OH background. At 5.5 C The K_s background is 13.6 mag arcsec^{-2}(Vega).

[3]Depths are defined to be the 5σ background fluctuations within a $0\farcs7$ diameter circular aperture in 1 hour (no correction for light outside the aperture). Total magnitudes for point sources in $0\farcs5$ FWHM seeing are approximately 0.7 mag brighter. The depths listed are for typical observing conditions and can vary, especially in H and K_s, by several tenths of a magnitude.

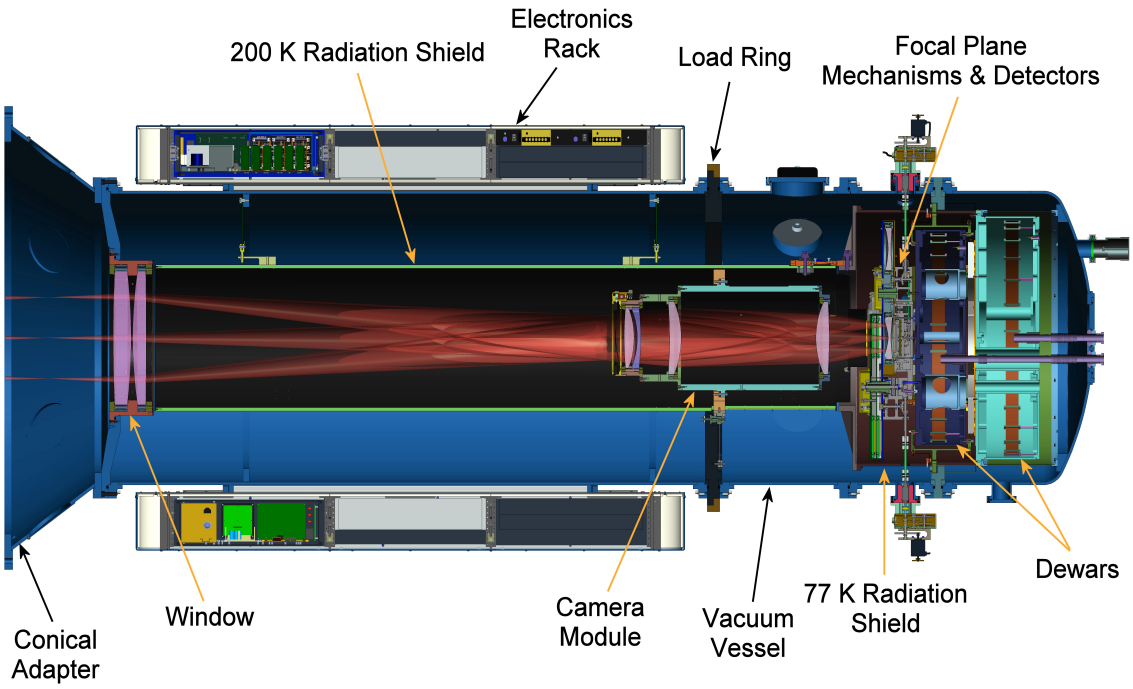

Fig. 1.— Cross-section view of FourStar. The optical path is shown in orange with light entering from the left. The conical adapter is bolted to the telescope's guider and instrument rotator. Most of the weight of the instrument is carried by the Load Ring through the Cart Rollers and to the Nasmyth platform of the telescope.

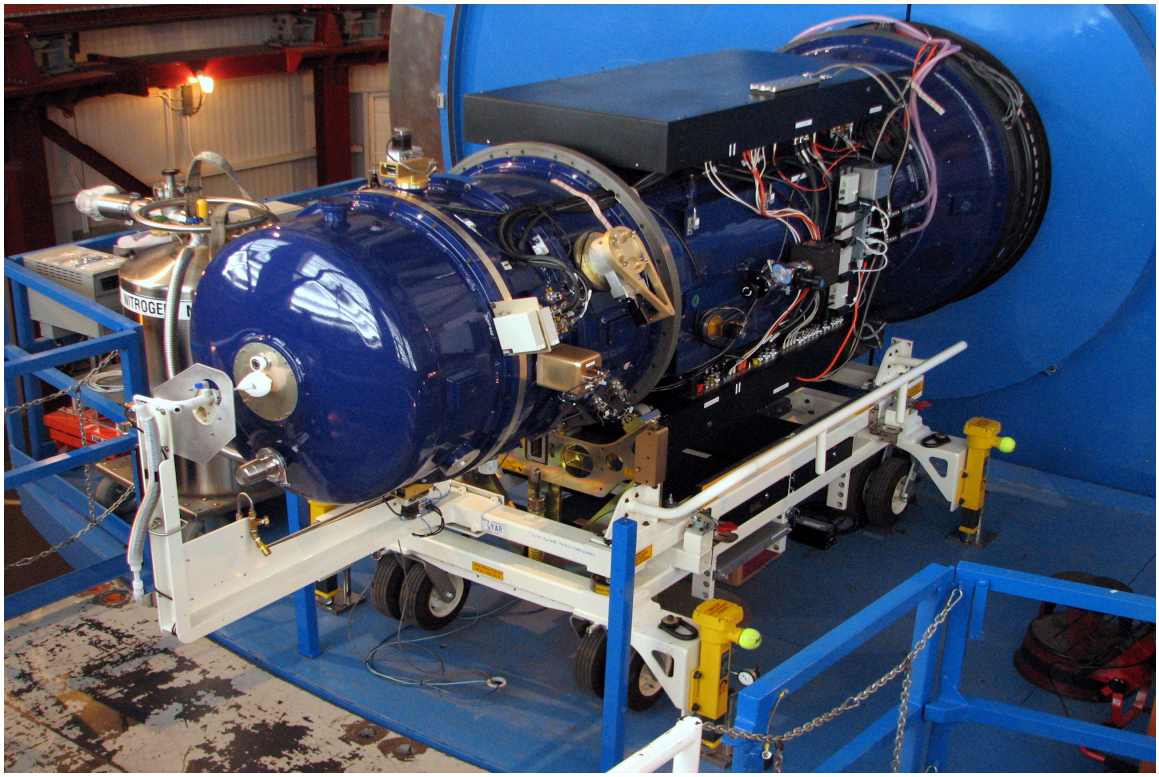

Fig. 2.— FourStar on the telescope, February 2011.

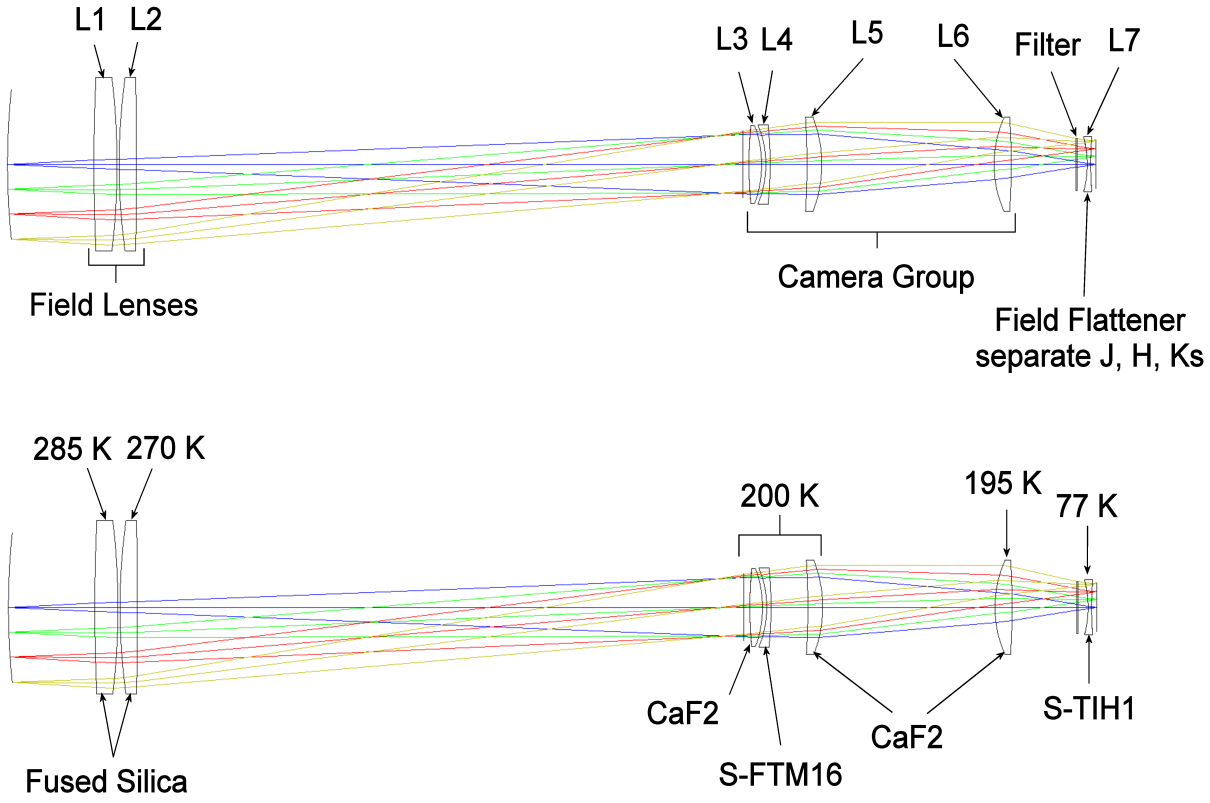

Fig. 3.— Optical layout showing (top) the lens identifications and (bottom) the temperature regimes and materials. Light from the curved telescope focal plane enters from the left and intersects the detector focal plane at the far right. The pupil plane, where the cold stop is located, lies just in front of the first CaF_2 element of the camera group; re-imaged rays from the telescope primary mirror can be seen intersecting there.

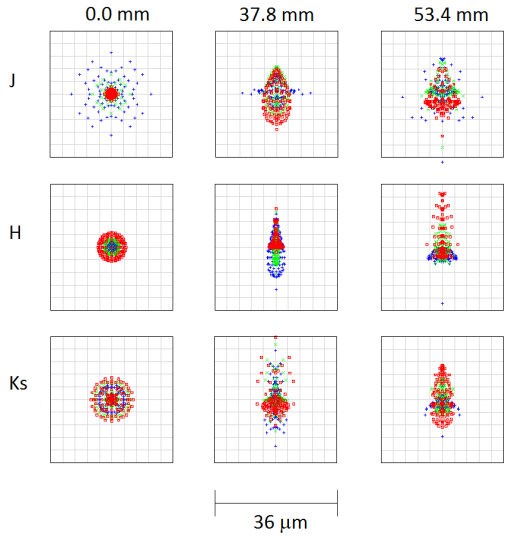

Fig. 4.— Spot diagrams in the image plane are displayed as predicted by ZEMAX for the J, H, and K_s passbands. Predicted spots are displayed for positions on-axis, at the edge, and corner of the detector mosaic footprint corresponding to radial distances of 0.0, 37.8, and 53.4 mm from the optical axis, respectively. The blue, green, and red symbols indicate rays traced at wavelengths correpsonding to the blue edge, center, and red edge of each passband, respectively. The 36 μm boxes are two pixels across.

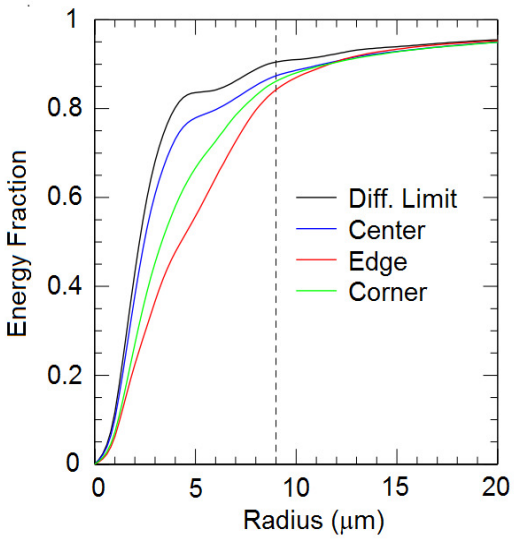

Fig. 5.— Polychromatic encircled energy plots predicted by ZEMAX for focal plane images. The black, blue, red, and green curves correspond to the diffraction limit, on-axis (center), edge, and corner of the square footprint of the detector mosaic, respectively. These correspond to radial distances of 0.0, 37.8, and 53.4 mm from the optical axis. The diffraction limit curve is computed by ZEMAX using the FFT method; see the ZEMAX manual for details. The vertical dashed line marks the edge of one pixel. 95% of the energy is captured within two pixels at all points in the detector mosaic.

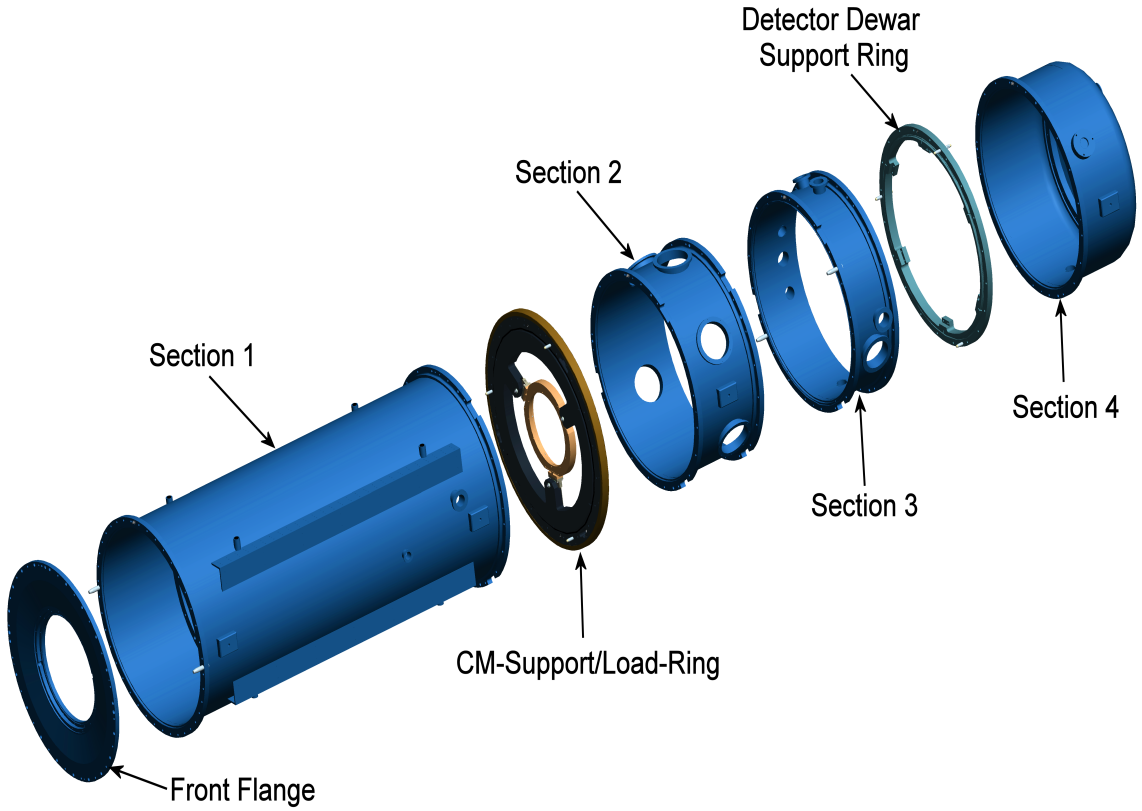

Fig. 6.— Exploded view of the vessel sections. All the circular parts are made from rolled and seam-welded 6061-T6 aluminum sheet. The window field lens assembly mounts on the Front Flange. The CM-Support/Load-Ring, referred to as the Load Ring in Figure 1, is aligned with the center of gravity of the CM. The holes in Section 2 are access ports for the cold clamps, temperature and pressure sensor plugs, and pump attachment hardware. The holes in the center of section 3 are aligned with the focal plane mechanisms; the various holes shown are for motor feedthroughs and hermetic electrical connectors.

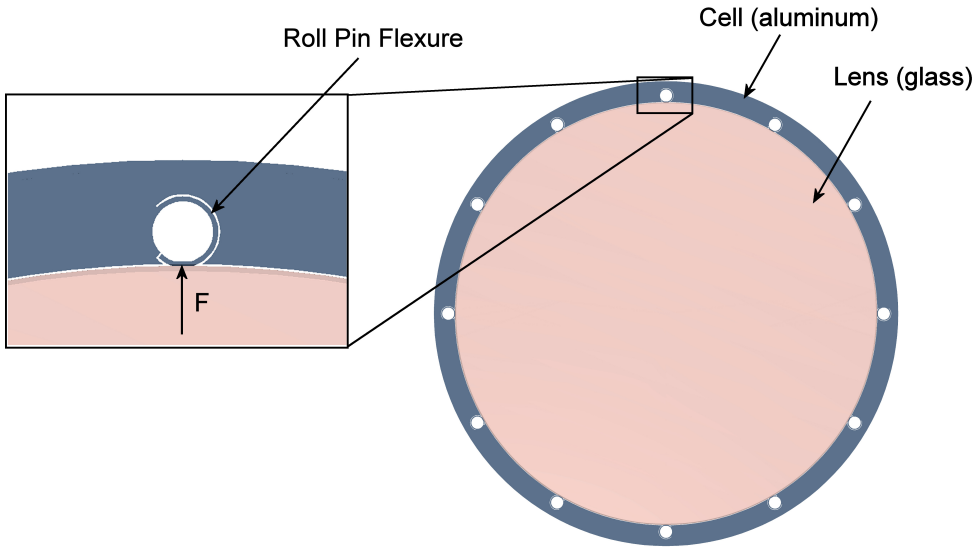

Fig. 7.— Roll pin flexure design, common to all lenses in FourStar. The compliant flexures, machined into an aluminum ring using wire-EDM, accommodate differential contraction between the cell and glass lens. The contour of the flexure conforms to the lens diameter, reducing contact stresses. Precision machining of the cell guarantees accurate centration without adjustment. Assembly of the cell and lens is accomplished by chamfering the flexures.

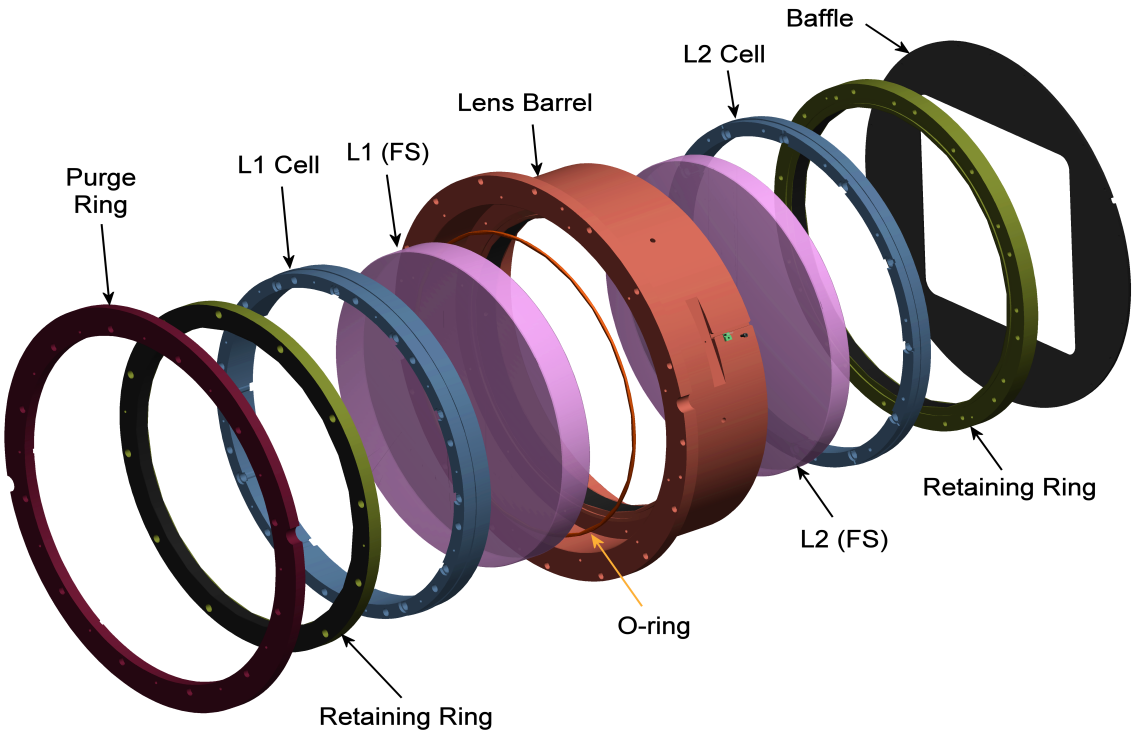

Fig. 8.— Exploded view of the window field lens assembly. It attaches to the front flange of the vessel (Figure 6). Lenses L1 and L2 are held by roll pin flexure cells as shown in Figure 7. The cells are screwed into the barrel. Retaining rings, screwed into the cells, clamp each lens onto a contoured ledge in its cell. The clamping forces were pre-determined and generated by a stack of Belleville washers. The L1 lens barrel holds two vacuum O-rings: one for the L1/barrel interface, the other for the barrel/front flange interface. The light baffle helps to reduce stray light. Dry air enters the purge ring and is blown over L1.

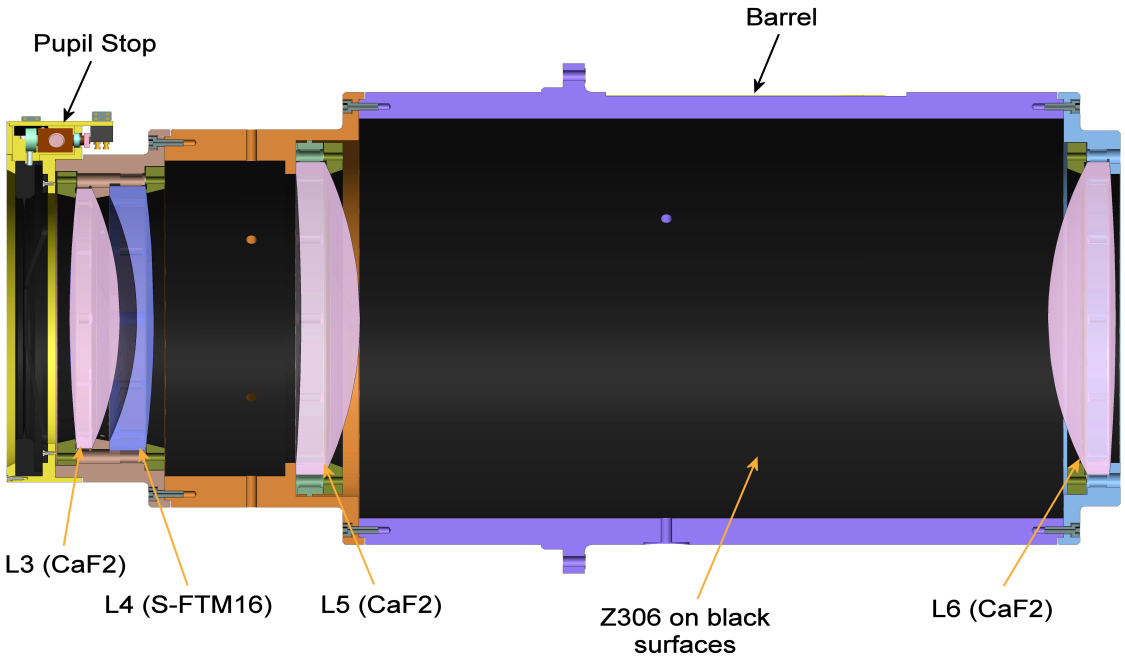

Fig. 9.— Details of the CM showing its four lenses. The barrel is comprised of three sections: lenses L3 and L4 are mounted in the left-most section, L5 in the center section, and L6 in the right-most section. Lens cell designs are as shown in Figure 7. Retaining rings are shown in olive green. The pupil stop design is discussed in §7.3.

Fig. 10.— A.M. and S.E.P shown inserting (via a crane/strap) the CM into the mylar-covered 200K shield within vessel section 1. The load ring is the gray ring at its end. The copper-colored rectangular patch on the body of the module is one of the three Minco heaters.

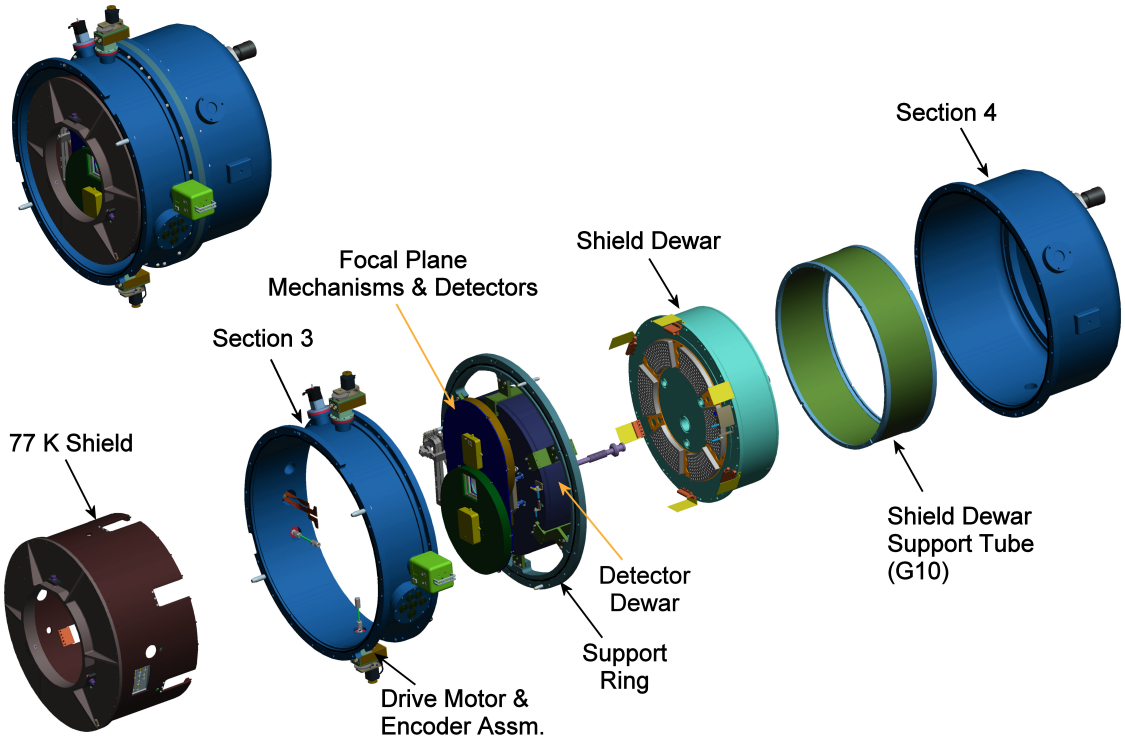

Fig. 11.— Exploded view of the back end assembly. Sections 3 and 4 of the vessel are shown in blue. The drive motor feedthroughs and wiring connect to the focal plane mechanisms and detectors through the walls of section 3 (see Figure 12). A stainless steel support ring holds the detector dewar via six G10 clamps (see also Figure 12). The shield dewar is supported by a G10 cylinder attached to the inside of section 4. The 77 K radiation shield, to the far left, attaches to the shield dewar.

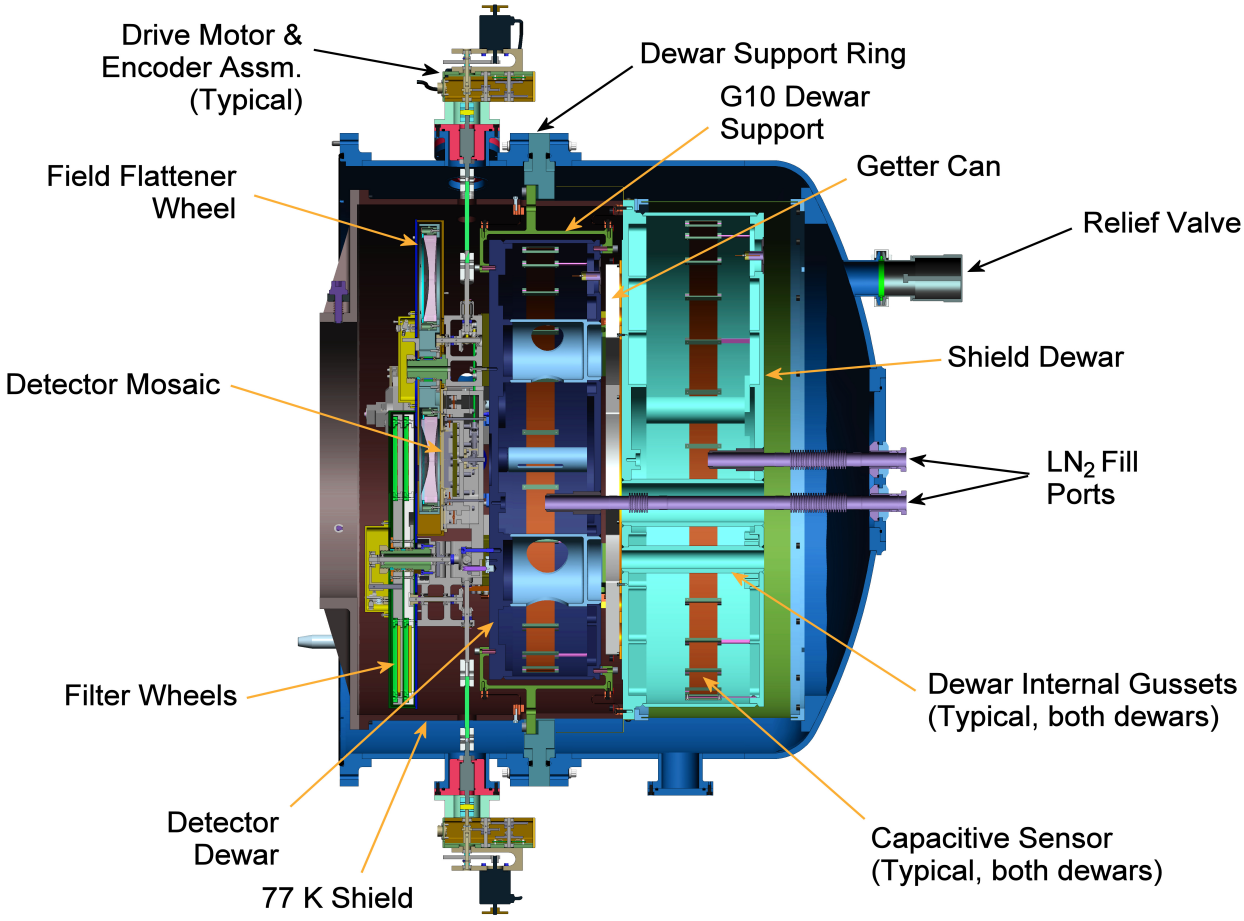

Fig. 12.— Cross section view of the back end. The 77 K cold shield, attached to the shield dewar, surrounds most of the detector dewar and focal plane region. Each dewar contains a capacitive sensor shown here as copper-colored strip.

Fig. 13.— The copper capacitor under construction and mounted on the aluminum back plate of the shield dewar before welding. The milled pockets in the back plate are for lightweighting.

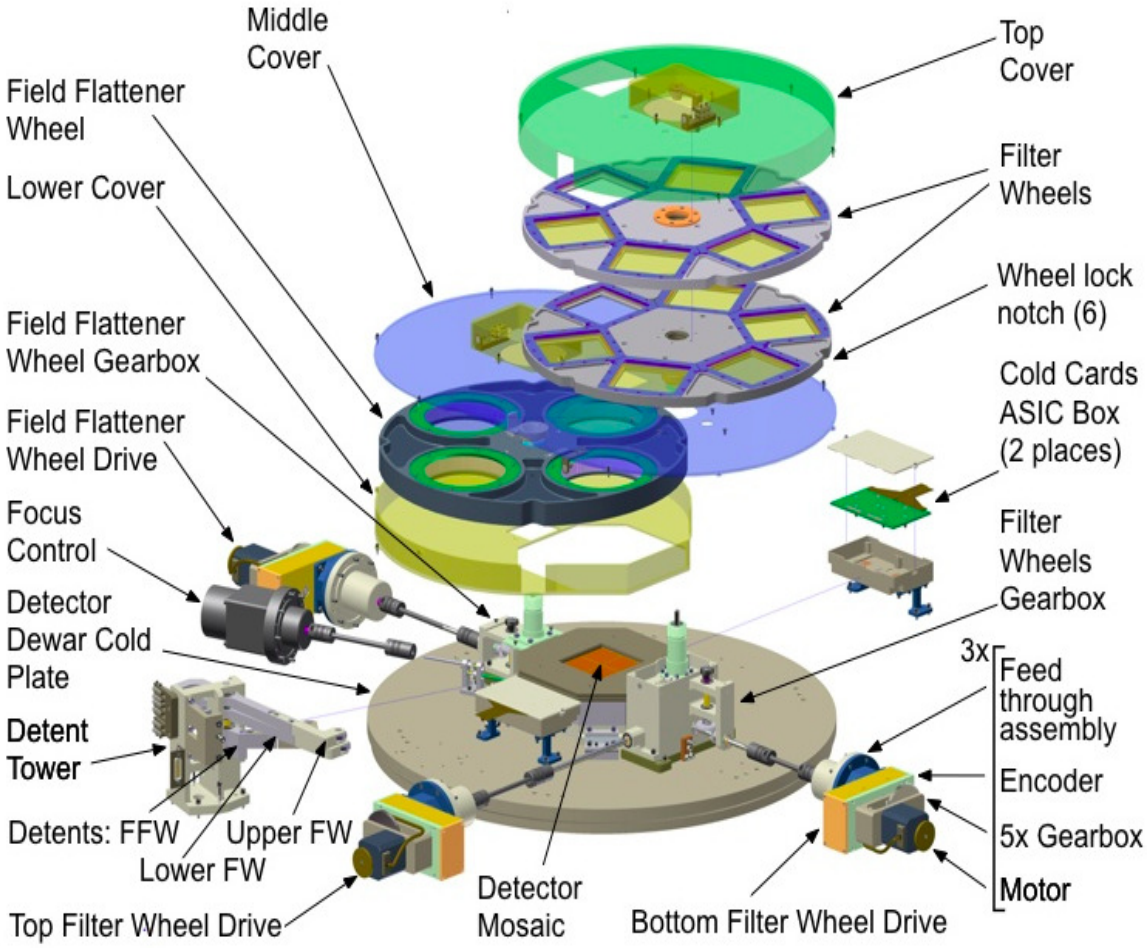

Fig. 14.— Detector dewar cold plate with detector module and wheels gearboxes attached, plus exploded view of the components. The detent tower holds three arms with ball bearings at each end. FFW indicates the Field Flattener Wheel. The bearing outer races roll into the 6 notches visible around the circumference of each wheel. The ASIC boxes are shown in both an exploded view and in a closed view.

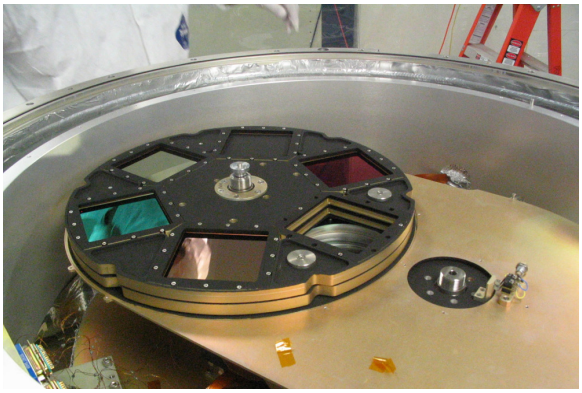

Fig. 15.— The two filter wheels shown with their top cover removed. The two large concentric cylinders are the Section 3 vessel wall and the 77 K radiation shield.

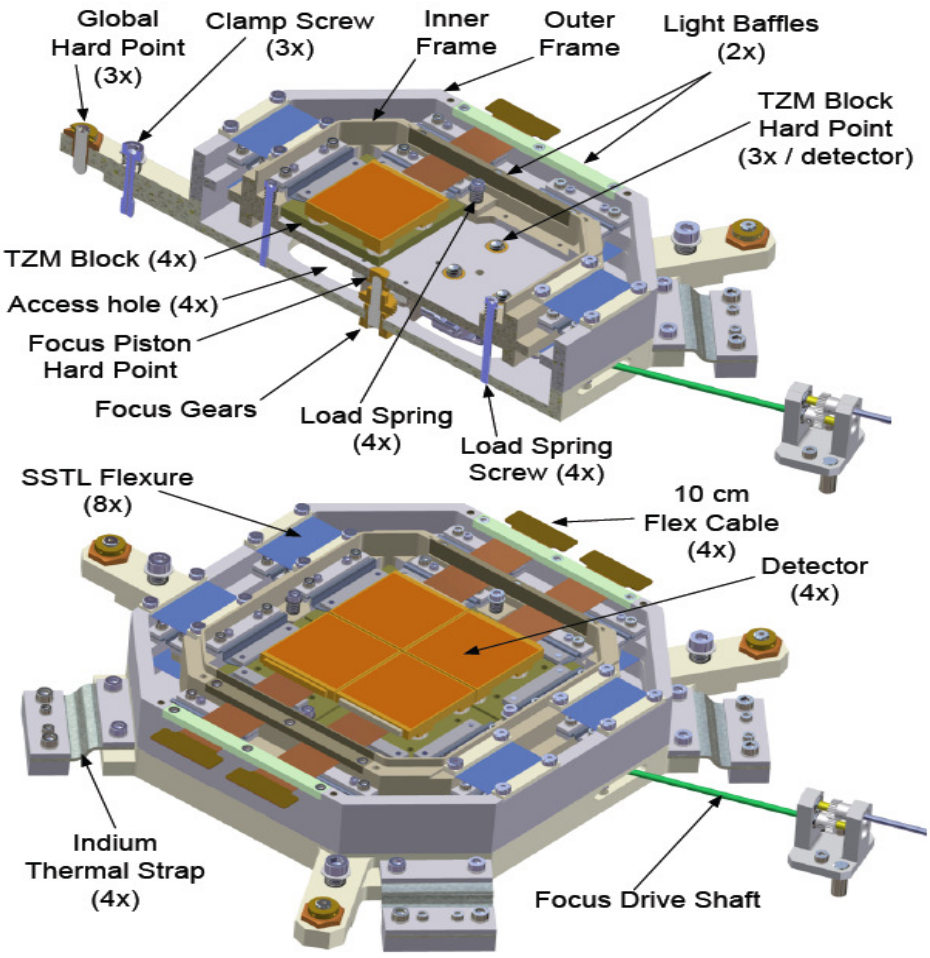

Fig. 16.— The top drawing shows a cutaway view of the detector module. One detector has been removed to show its three hardpoints, each adjustable from behind the module through the access holes. Indium straps provide thermal contact between the frames but are hidden in this view. The top of the module is covered by a plate used to reduce scattered light, but not shown for clarity. The bottom drawing shows the entire module.

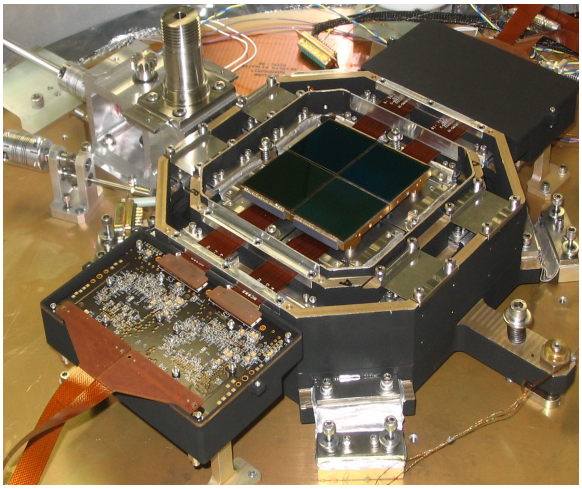

Fig. 17.— The detector module is shown attached to the surface of the detector dewar. The four black squares are the detectors. The PCB flex cables connect in pairs to a single Cold Card. One is shown mounted within its rectangular black box, shown open at bottom left; the other is hidden within its box, shown closed at upper right. The PCB flex cables (one pair shown at lower left) connect to a hermetic connector.

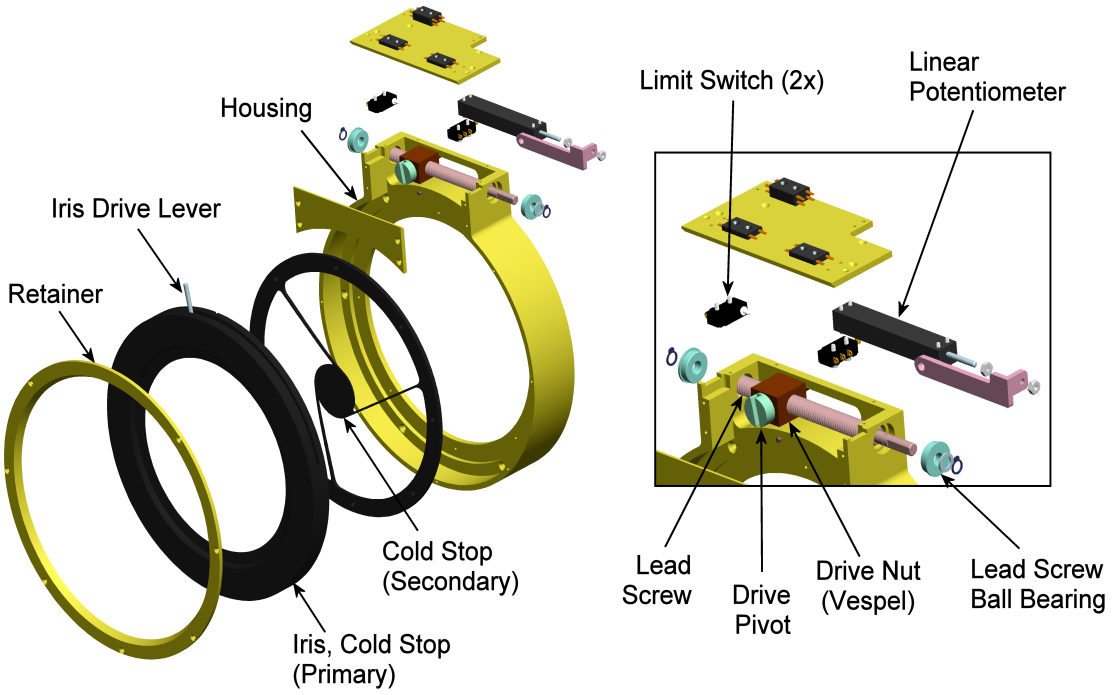

Fig. 18.— Exploded view of the cold stop, consisting of the stop for the image of the edge of the primary mirror, and that for the secondary. The K_s image of the primary mirror is at the axial position of the stop, defined by an iris. The iris is composed of blades captured within two rings. Its open dimension, changed by operating the drive lever, is closed down to a fixed opening for observations with the K_s filter and opened wide for the rest. The iris drive ring was hard coat anodized with a polytetrafluoroethylene (PTFE) impregnation to reduce friction. The drive mechanism details are shown in the box. A driveshaft, turned from outside the vessel, causes the drive nut to move along the lead screw. This nut/drive pivot captures the iris drive lever. At the same time, the drive nut causes linear motion of the shaft of a precision potentiometer. The variable resistance is measured and converted to a position. Limit switches wired into the drive circuit protect the mechanism from collisions of the drive nut with the housing.

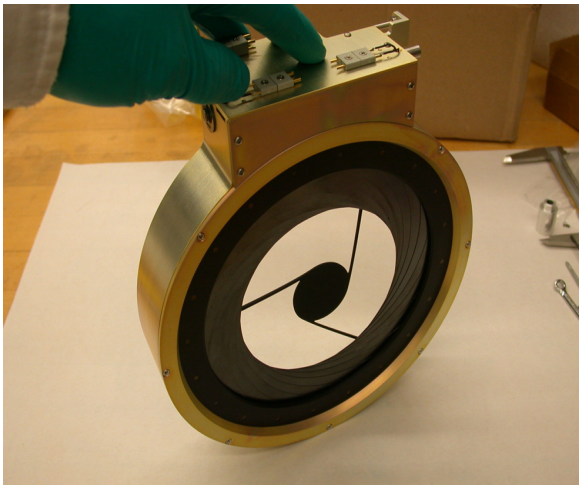

Fig. 19.— Photograph of the completed pupil stop mechanism. Not shown, but attached to the front of the housing, is an annular baffle (painted with Z306) that is 50% larger than the housing. It is used to block diffuse/scattered light that might otherwise get past the mechanism. The three spiders holding the central black disk (see also Figure 18) are curved so that they never align with the secondary mirror spiders. This would cause a small change in the K_s background.

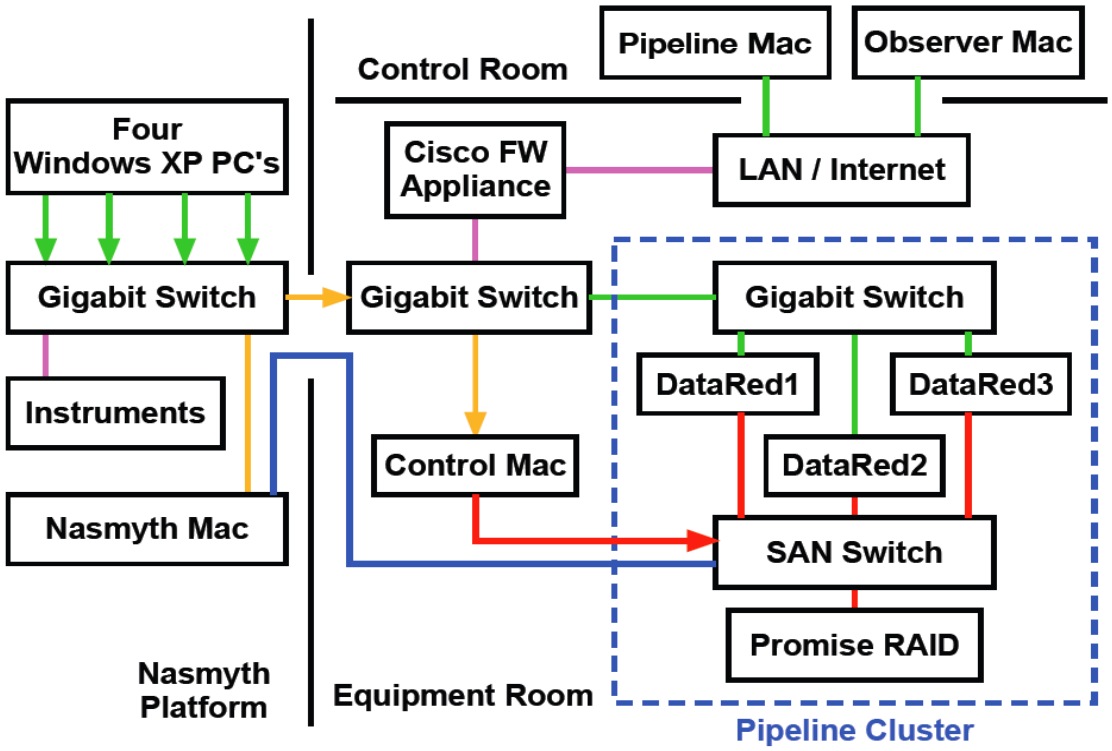

Fig. 20.— The main elements of the Four-Star control system. The data paths are color coded: 100 Mbs^{-1} copper Ethernet (magenta), 1 Gbs^{-1} copper Ethernet (green), 1 Gbs^{-1} fiber optic Ethernet (yellow), 4 Gbs^{-1} fiber optic Fibre Channel (blue), and 4 × 4 Gbs^{-1} trunked copper Fibre Channel (red). The Control Mac initiates acquisition of data from the Windows XP PCs. The Control Mac is accessed remotely via the Observer Mac in the control room. Arrows mark the data path traversed for high-speed acquisition of imaging data via fiber optics and trunked copper cables. Raw image frames from the detectors stream via the Windows XP PCs, through the acquiring Control Mac, directly to the Promise RAID drive of the pipeline reduction cluster, shown enclosed in a blue dashed line box. The pipeline cluster is formed by the Promise RAID drive and server computers DataRed1, 2, and 3 linked to each other via Ethernet and Fibre Channel-based Storage Area Network (SAN). The Control Mac and its backup, the Nasmyth Mac, are clients of the cluster and as such have shared high-speed access to the RAID drive. For simplicity the metadata network is not shown. The real time reduction software runs continuously on the 24 processing cores of the three-server pipeline cluster.

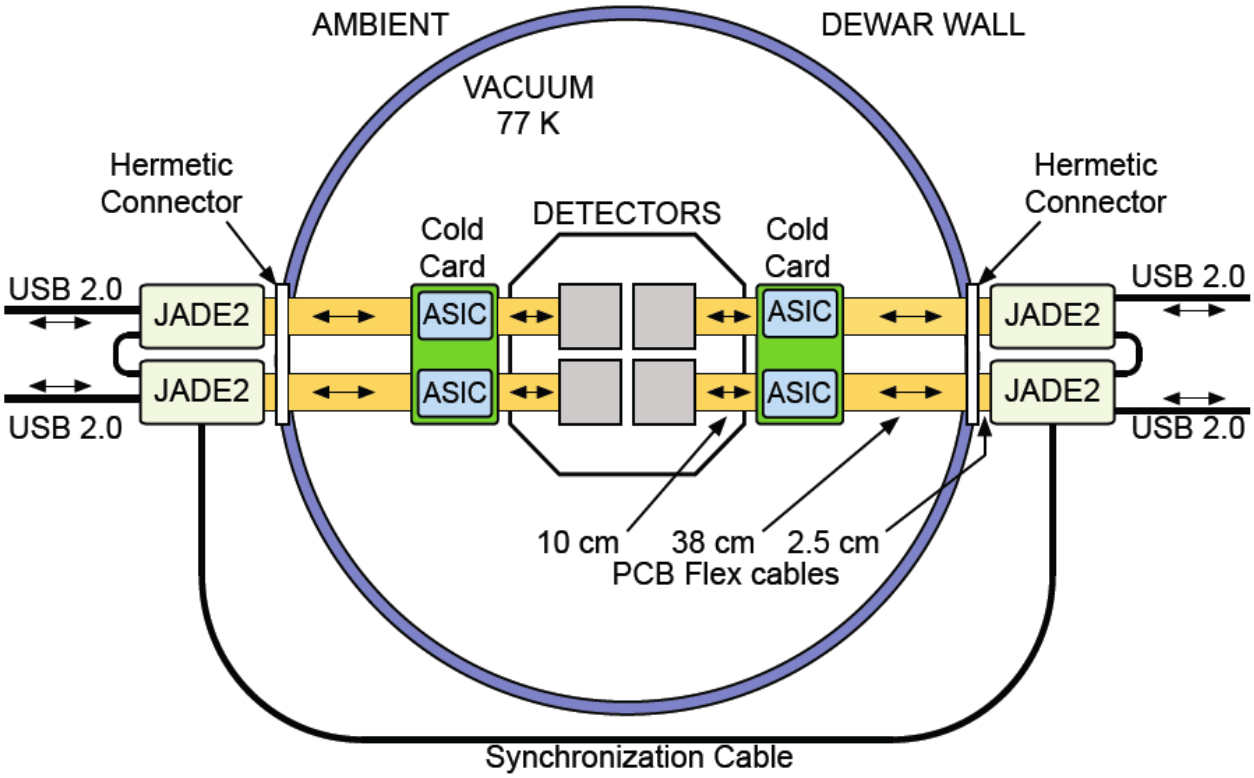

Fig. 21.— Sketch/block diagram of the detector/ASIC/JADE2 signal chain. The four gray squares are the detectors, two on each side of the detector module octagonal mounting frame. Each pair of detectors connect via two 4 cm PCB flex cables to two ASICs mounted on a single Cold Card. Each Cold Card is connected via two 38 cm PCB flex cables to a Micro-D hermetic connector. Short (2.5 cm) PCB flex cables on the ambient side connect to two JADE2 cards which interface via USB 2.0 to two PCs. The synchronization cable busses clocks and trigger signals from a master JADE2 card to the other three. This mitigates beating clock signals.

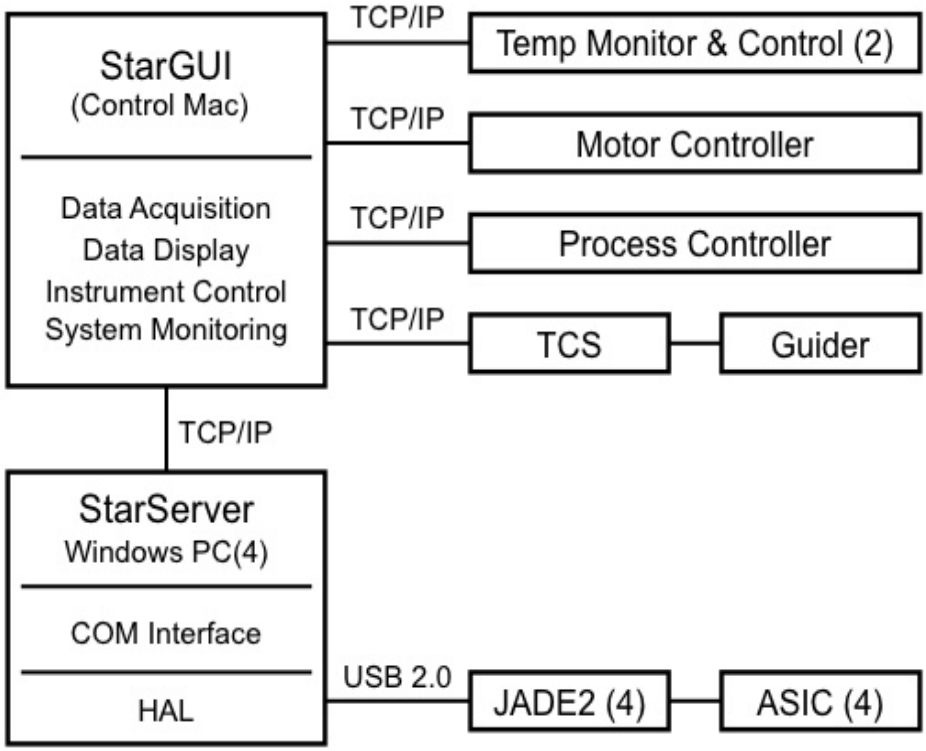

Fig. 22.— Block diagram of the control system software. StarGUI, which runs on the Control Mac, controls and and monitors all functions of the instrument. StarServer, which runs on the Windows PCs, controls the four detectors. TCS is the telescope control system.

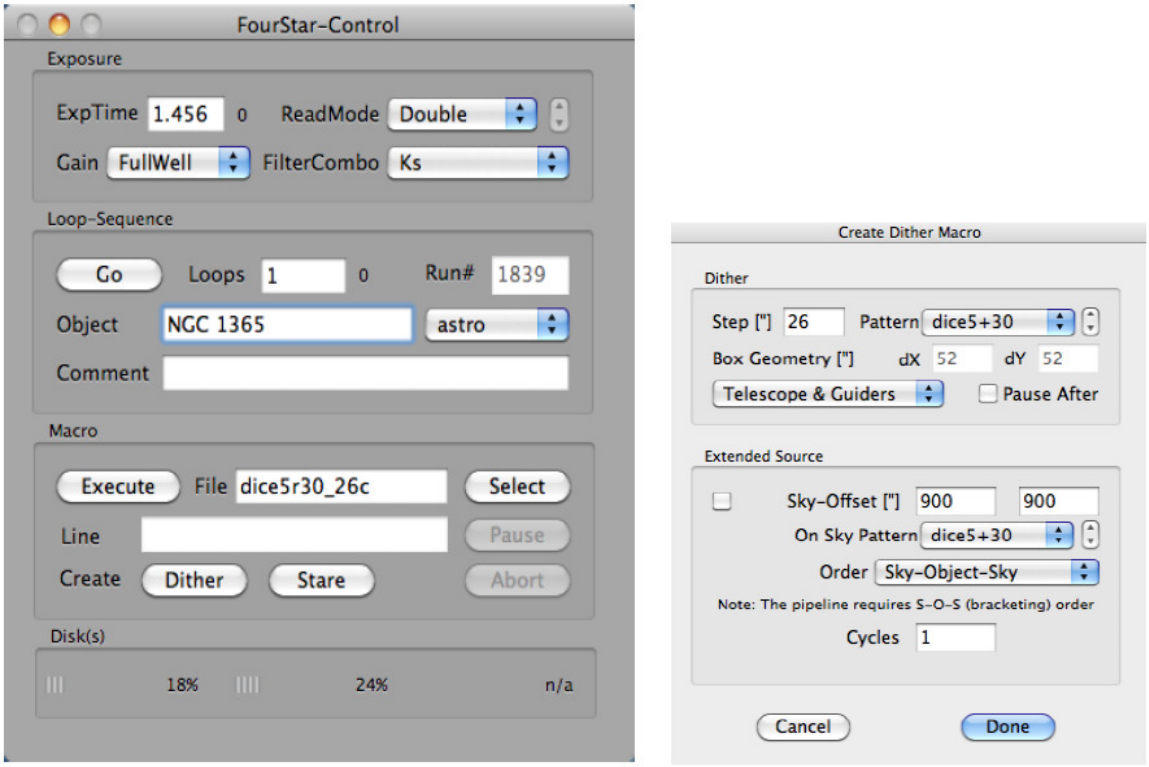

Fig. 23.— Camera control and macro creation tools. The control window has three panels: Exposure setup, Loop sequences and Go button, and Macro information and Macro Execute button. Macros are created in the right-hand Create Macro window.

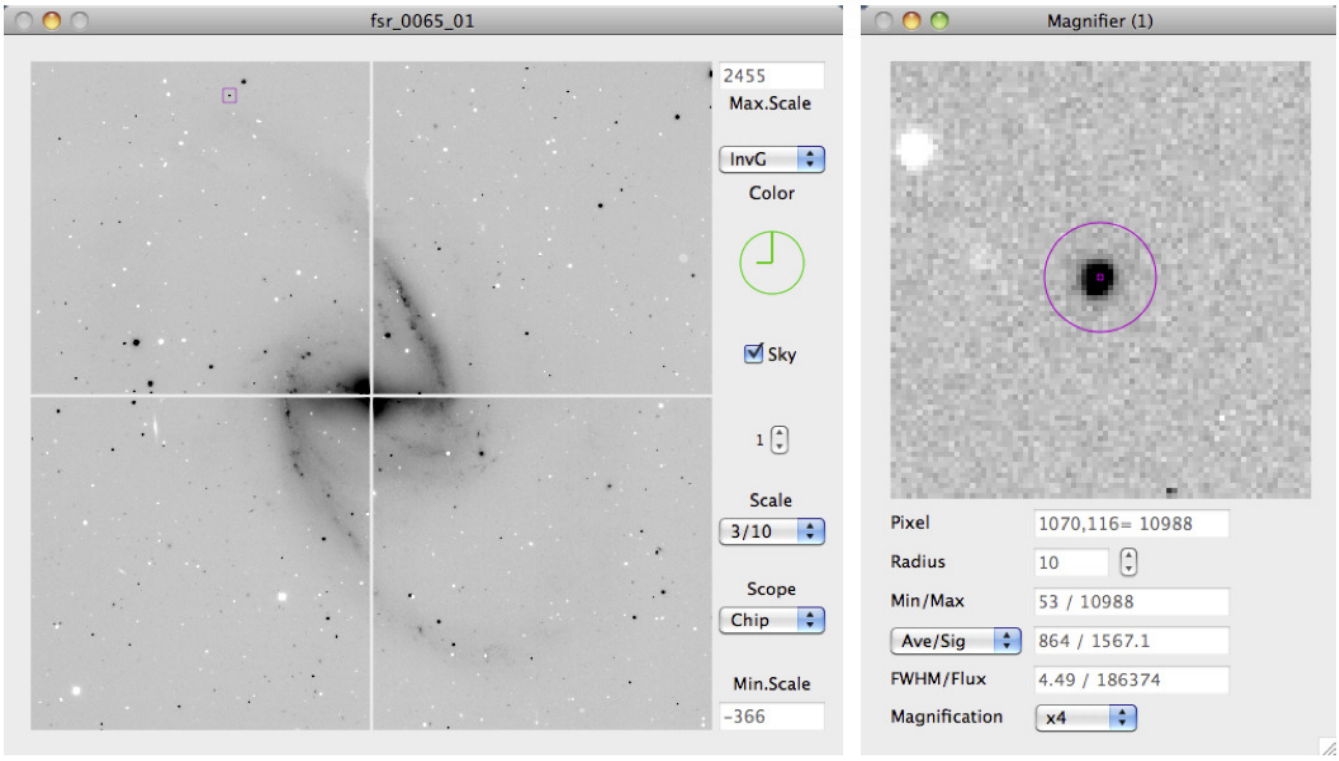

Fig. 24.— Quick look and Magnifier windows. The white stars in this first light image of NGC 1365 are due to the simple sky subtraction scheme used. The Magnifier window on the right allows the observer to zoom in to arbitrary locations on the quick look image.

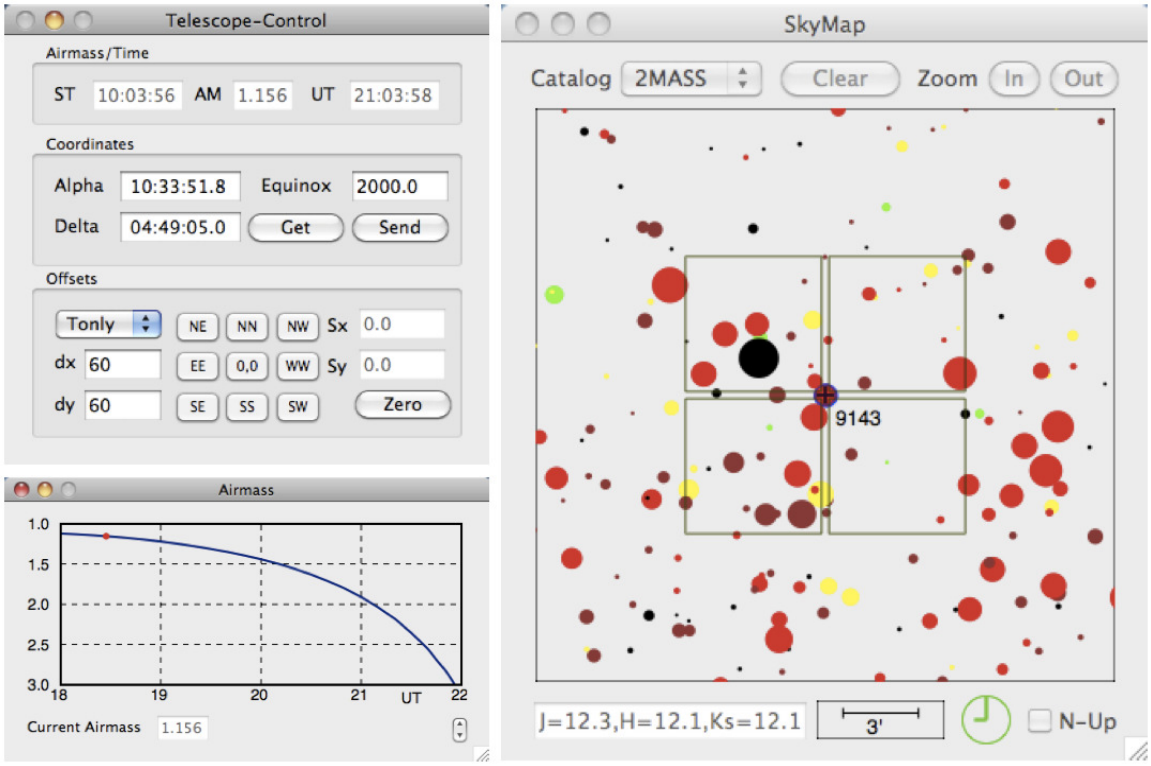

Fig. 25.— Telescope Control, Airmass display, and SkyMap windows. The four square boxes in the SkyMap window represent the four detectors. Star maps from a selection of catalogs can be displayed.

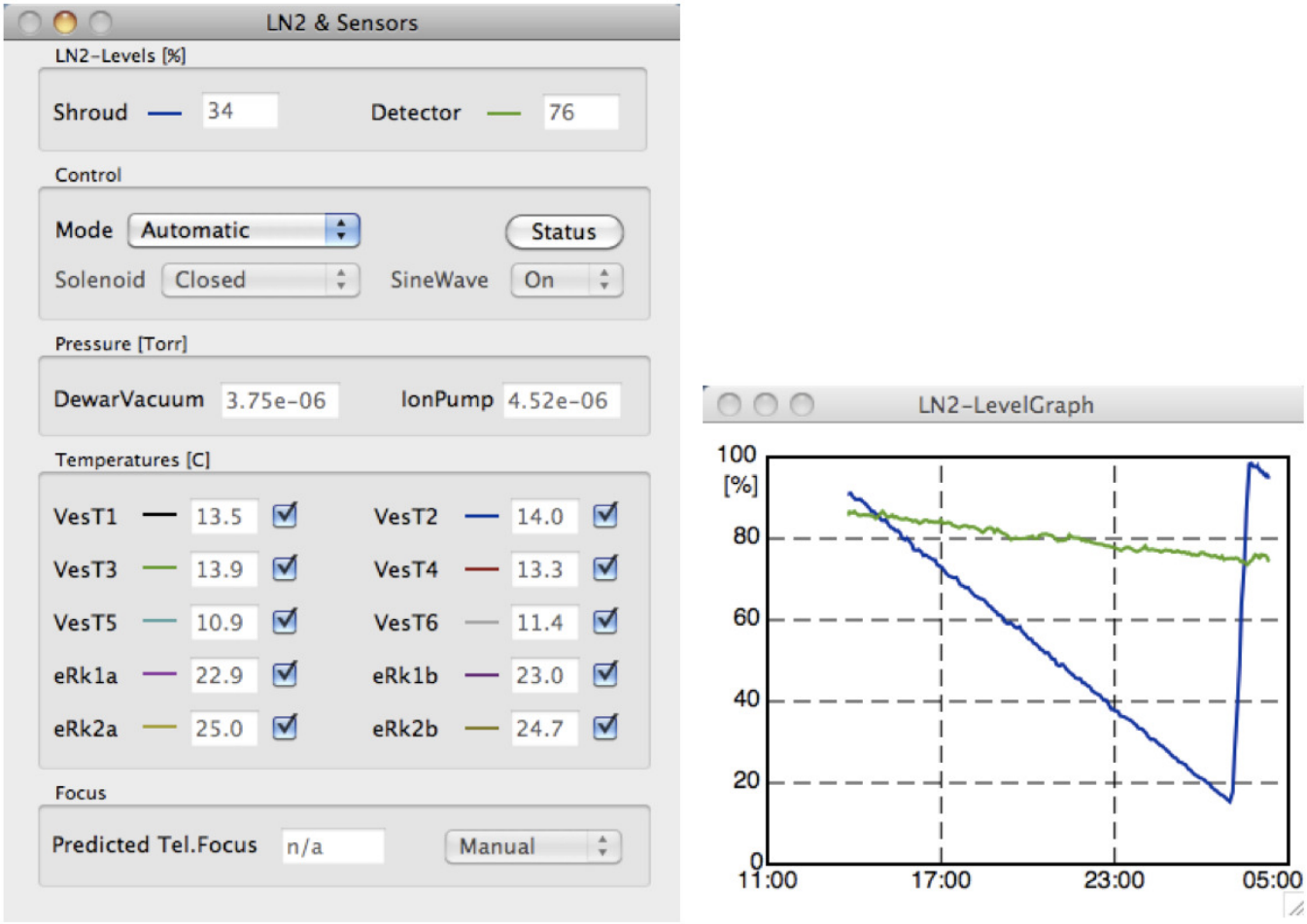

Fig. 26.— Process controller GUI. On the left are the LN_2 levels, the LN_2 fill solenoid status, the vessel pressure, and the vessel and rack temperatures. On the right is a graphical display of the LN_2 levels as a function of time. Note the filling of the shield dewar at 03:00.

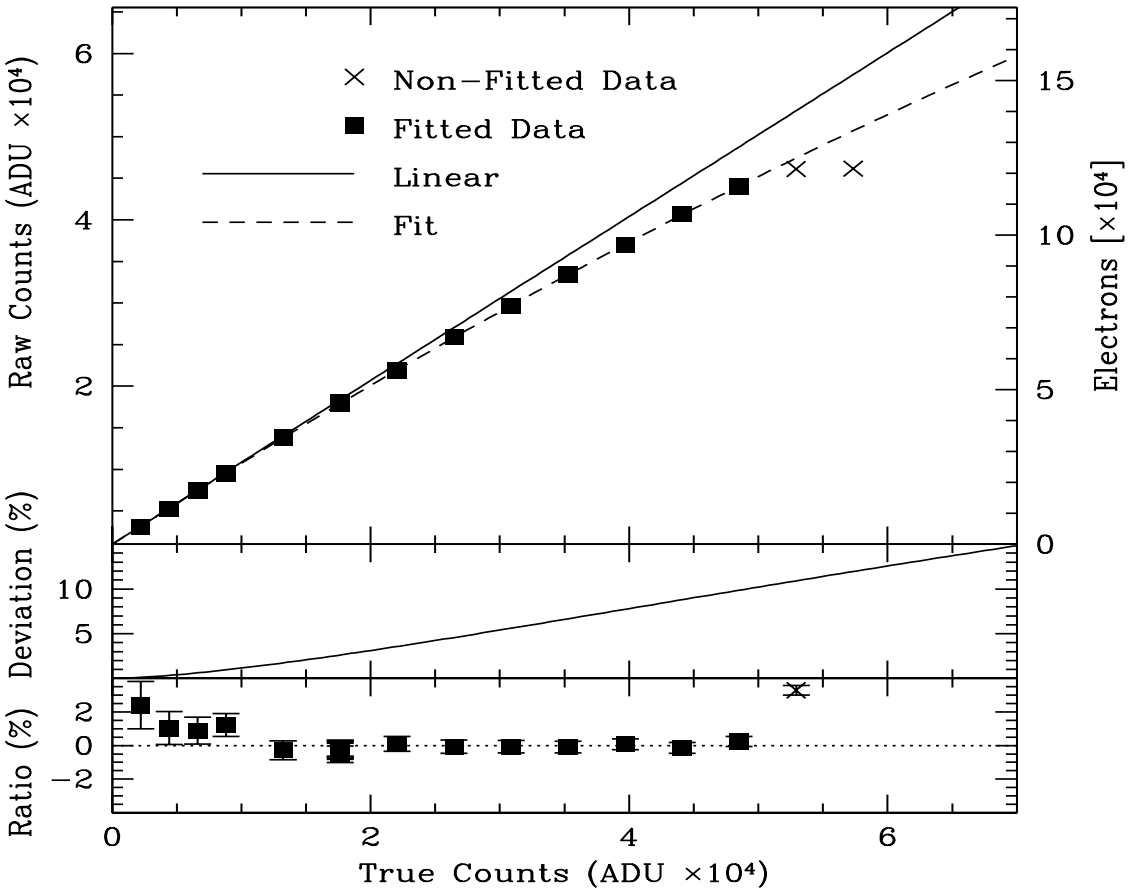

Fig. 27.— Linearity plot for one pixel in the FullWell gain setting. The squares in the top panel show the measured (raw) counts versus the true counts in ADU. The fitted curve has the functional form: $\mathrm{ADU}_{true} = \mathrm{ADU}_{meas}(1. + \mathrm{A} \times \mathrm{ADU}_{meas}^{1.5}) + \mathrm{B}$. For this particular pixel $\mathrm{A} = 1.253 \times 10^{-8}$ and $\mathrm{B} = 0$. The middle panel shows the % deviation of the two curves. The bottom panel shows the % deviation of the data from the fit. The simple parametric form of the correction equation works well up to 43,000 ADU_{meas}, which is 48,000 ADU_{true}, or 120,000 e^-. These values correspond to a correction of $\sim 10\%$.

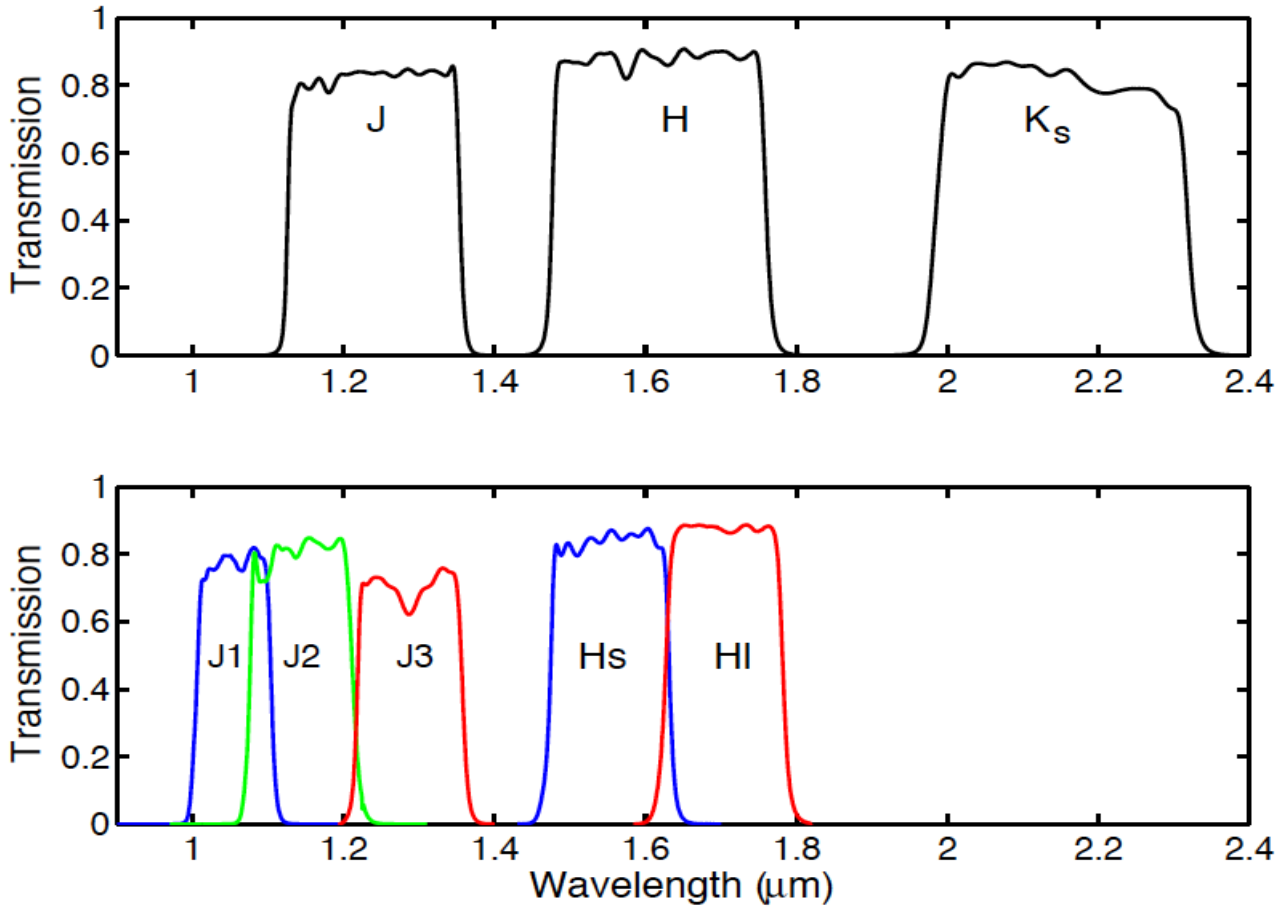

Fig. 28.— Instrument passband profiles including lenses L1 - L7 and the broad- and medium band filters. The NB119 and NB210 profiles are too narrow to be shown at this scale. Profiles in digital form can be found on the instrument website.

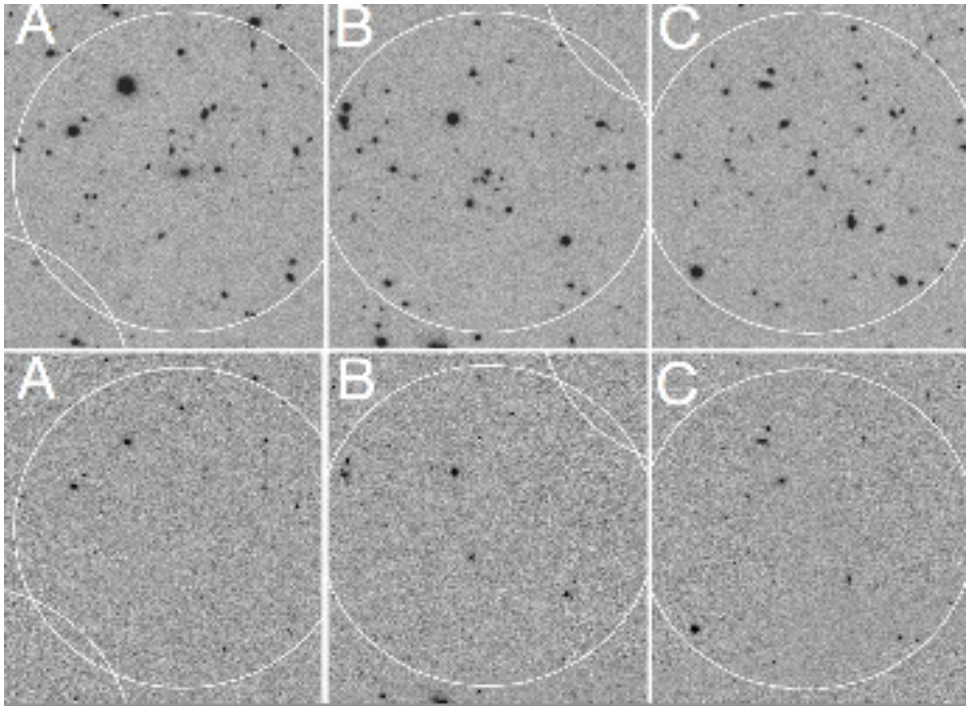

Fig. 29.— Comparison of FourStar K_s images (upper three; 10 hour exposure) with HST I-band images (lower three; 1 hour exposure). The fields are concentrations A, B, and C from the Z-FOURGE discovery of a mature galaxy cluster at z $\approx$ 2.2 (Spitler et al. 2012). Note how the red galaxies in the cores are barely seen in the I band, but are easily measured in K_s. The circles are $1'$ in diameter.

Fig. 30.— FourStar two-color composite (J= blue, K_s = red) of the galaxy M83. The individual frames are being used to obtain photometry of Cepheids as part of the CHP program (Freedman et al. 2011).

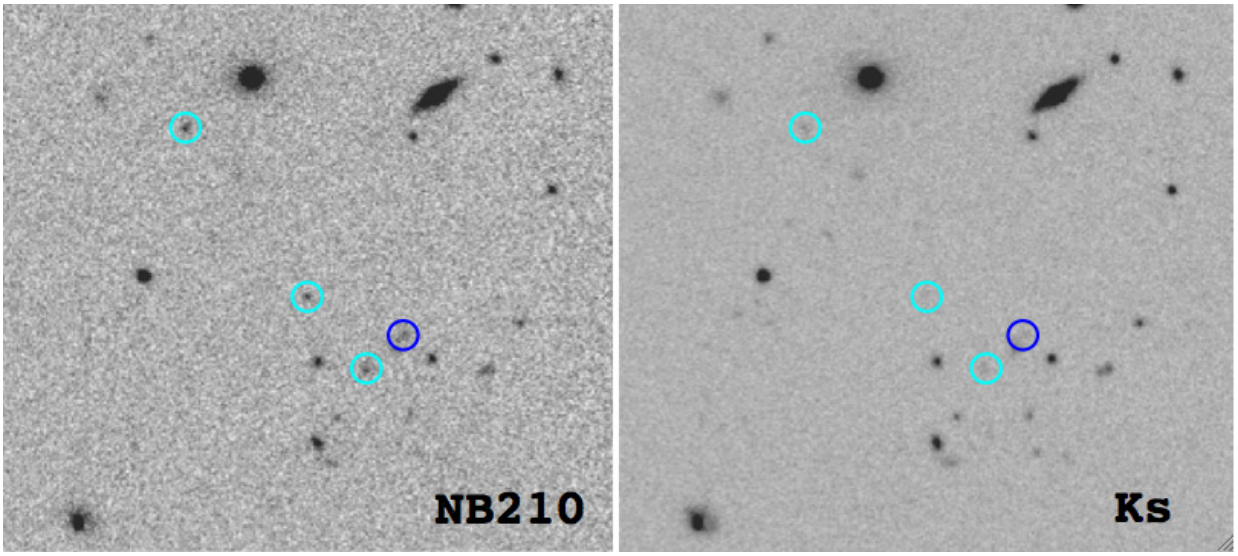

Fig. 31.— Comparison of narrow band NB210 and broad band K_s images. The objects identified by the cyan circles have excess emission compared to the K_s continuum, indicating an emission line. That the line is Hα is confirmed by an emission line in the NB119 filter; it is due to [OIII]λ3727 at the same redshift of 2.2. The object in the dark blue circle also has a narrow-band excess, but it lacks a confirming line in the NB119 filter. The area is a $25'' \times 25''$ cut-out, and the circles are $1.2''$ in diameter. At z $\approx$ 2.2, these scales correspond to 200 and 10 kpc, respectively. The images represent 8.4 and 5.8 hours of exposure time in the NB210 and K_s filters, respectively.